

Chapter 1

Introduction

1.1 A brief review of ferroelectric material and perovskite

1.1.1 Ferroelectric material

Ferroelectricity is a phenomenon such as a spontaneous polarization on cooling below the Curie Point, ferroelectric domains, a ferroelectric hysteresis loop and so on. Ferroelectric ceramics were born in the early 1940s with the discovery of the phenomenon of ferroelectricity as the high dielectric constant in barium titanate (BaTiO_3). Ferroelectric materials have long been used in bulk form in a variety of fields. Today, ferroelectric materials are deposited in thin films and they are essential materials for a variety of devices such as ferroelectric random access memory (FRAM), infrared pyroelectric sensors, transistors, microwave electronics, electro-optic modulators and other integrated devices. Among the many classes of ferroelectric materials, the perovskite compounds such as the lead lanthanum titanate (PLT) [1], lead zirconate titanate (PZT) [2], lead titanate (PT) [3], and barium titanate (BT) [4] have been the most intensively investigated.

1.1.2 Perovskite

The perovskite compounds are an extremely important group of ferroelectric materials. The general formula of perovskites is ABX_3 (see Fig. 1.1), which is

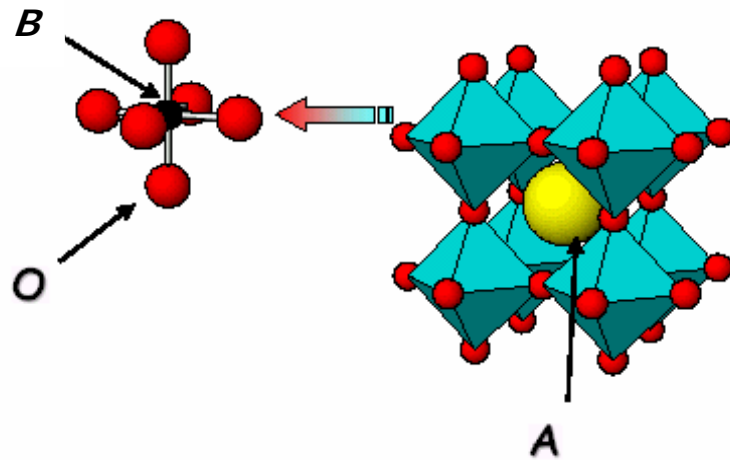


Figure 1.1 perovskite structure

composed of three distinct chemical elements in the ratios of 1:1:3. The “A” and “B” atoms are metallic elements and the “X” atom is a non-metallic element. The “A” metallic atom is usually larger than “B” metallic one in the perovskite structure. The “A” and “B” atoms represent +2 and +4 ions, respectively, while the “X” atom is the O⁻² ion. The ABO₃ structure in a general sense can be thought of as a face-centered cubic (FCC) lattice with “A” atoms at the corners, the Oxygen atoms on the faces and the “B” atom at the center of the lattice (see Fig. 1.2). As the stronger electric field is applied to ABO₃-type perovskite, the “B” cation is more energized and farther from the original octahedron. Shifting of this atom due to applied electric field causes the structure to alter, thus to induce electric dipole.

The atomic structure of perovskite is very sensitive to the alteration in the temperature of the crystal. As the temperature changes, the crystallographic dimensions change due to distortion of the octahedral. The crystal structures of ABO₃ include cubic, tetragonal, orthorhombic, and rhombohedral [5] (see Fig. 1.3). All of

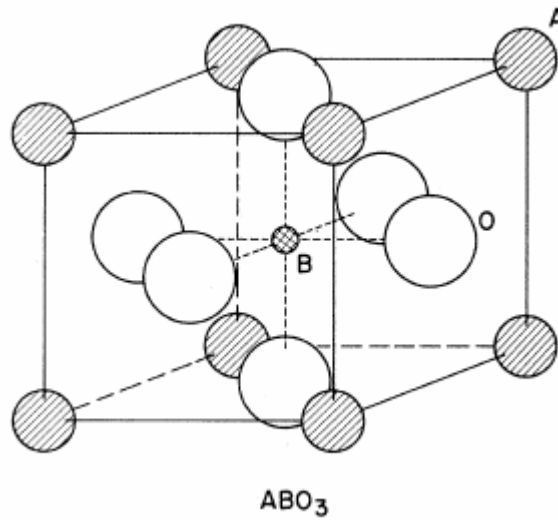


Figure 1.2 ABO₃ structure

the ferroelectric materials have a transition temperature called the Curie point (T_c). When the crystal temperature goes above the curie point, $T > T_c$, the crystal doesn't exhibit ferroelectricity, while for $T < T_c$ it is ferroelectric. On decreasing the temperature through the Curie point, a ferroelectric crystal undergoes a phase transition from a non-ferroelectric phase to a ferroelectric phase. As a result, the distorted octahedral are coupled together, and a very large spontaneous polarization can be achieved. This large spontaneous polarization will lead to a large dielectric constant highly sensitive to temperature.

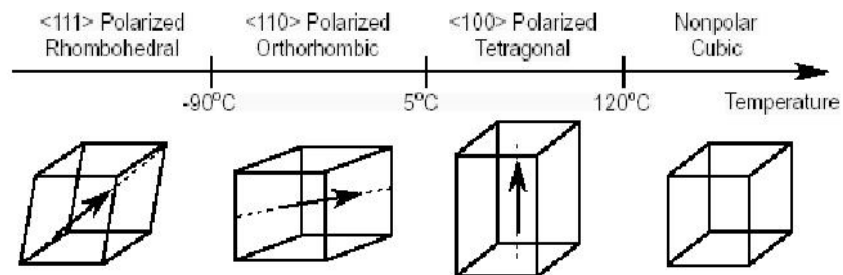


Figure 1.3 Phases of BaTiO₃

1.2 Rare-earth ion doped materials

Study on the luminescent properties of rare-earth ion doped materials is strongly motivated because of their potential applications in photonic devices and next-generation flat-panel displays. Rare-earth ions exhibit luminescence from electronic transition of a characteristic intra-4f shell that is nearly independent of both host material and temperature [6] (see Fig. 1.4). This feature can be used to tune the position of frequency of emission for specific applications. Thus, it is important for systematic research on the rare-earth ions doped in different kinds of host materials with good mechanical, thermal, electrical, and electro-optical properties. Lately, erbium-doped materials have been extensively studied because of the blue ($^2H_{9/2} \rightarrow ^4I_{15/2}$), green ($^4S_{3/2}, ^2H_{11/2} \rightarrow ^4I_{15/2}$) and red ($^4F_{9/2} \rightarrow ^4I_{15/2}$) up-conversion emissions. The laser actions have been realized in a variety of glasses and fluoride crystals [7-10].

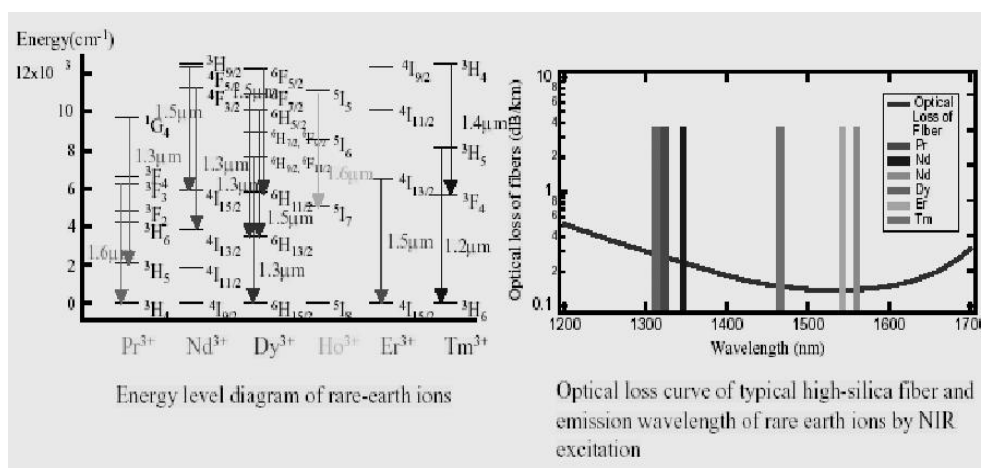
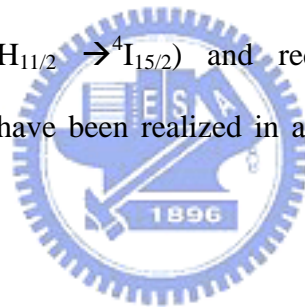


Figure 1.4 Energy level of rare-earth ions

1.3 Motivation

1.3.1 $\text{Pb}_{1-x}\text{La}_x\text{TiO}_3$ thin films

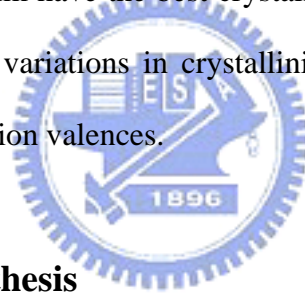
The ferroelectric transition occurs as a result of balance between long-range Coulomb interaction and short-range forces [11]. Particularly, the Coulomb interaction makes the ferroelectric sensitive in response to details of domain structure, defect, and boundary conditions. Another direct effect of such interaction is the splitting of longitudinal optical (LO) and transverse optical (TO) phonons. The Born dynamical effective charges play a central role in the study of these Coulomb effects. However, early calculations do not directly address the role of Coulomb interactions until giant LO-TO splitting has been performed in ABO_3 cubic perovskite compounds using local density approximation (LDA) by Zhong et al [11]. Previously studying on $\text{Ba}_x\text{Sr}_{1-x}\text{TiO}_3$ (BST) system [12], we have reported the repulsion of giant LO-TO splitting when tetragonal to cubic phase transition occurs, and it is explained as a result of decreasing cell dimension and strengthening the electron-phonon coupling, which was the first experimental evidence for the lattice dynamics related to the Coulomb interaction. Recently contrast to the increase of giant LO-TO splitting in $\text{Ba}_{1-x}\text{Sr}_x\text{TiO}_3$ (BST) system, a direct observation of the decrease splitting of $A_1(1\text{TO})$ and $A_1(3\text{LO})$ modes was reported in $\text{Pb}_x\text{Sr}_{1-x}\text{TiO}_3$ system [13].

Following the research of PST ($\text{Pb}_{1-x}\text{Sr}_x\text{TiO}_3$) system was reported earlier [13], we replaced the Pb^{+2} cations by La^{+3} with different ion radius, and valences respectively, forming $\text{Pb}_x\text{La}_{1-x}\text{TiO}_3$ (PLT). When PbTiO_3 is modified by La^{+3} ions, cation vacancies are created to keep the charge neutrality. Although on $\text{Pb}_x\text{Sr}_{1-x}\text{TiO}_3$ system, Pb-O interaction is proposed to be more hybridized than Ba-O, and thus the change of effective charge to the LO-TO splitting may be the dominant mechanism, not unit-cell

volume change [13]. We developed an interest in the influence of cation vacancies on the unit-cell volume change to the LO-TO splitting.

1.3.1 Er-doped $\text{Pb}_{0.8}\text{La}_{0.2}\text{TiO}_3$ thin films

Following the research of erbium-doped barium strontium titanate thin films [14], we used lead lanthanum titanate as candidate for a rare-earth doped host material. In addition to the virtue of barium strontium titanate such as high dielectric constant, small dielectric loss and low leakage current, lead lanthanum titanate has high optical transparency (>70%) in the visible wavelength region [15]. There are two advantages for using $\text{Pb}_{0.8}\text{La}_{0.2}\text{TiO}_3$ as the host material. First, the sol-gel derived lead lanthanum titanate ($\text{Pb}_{1-x}\text{La}_x\text{TiO}_3$) thin film have the best crystallinity at $x=0.2$ [15]. Another, its structure only showed slight variations in crystallinity, while we replaced the La^{+3} cations by Er^{+3} with the same ion valences.



1.4 Organization of the thesis

There are five chapters in this thesis. In Chapter 2, we first describe the related theoretic background such as lattice structure, lattice dynamics, and emission spectrum of energy levels of Er^{+3} -doped thin film. Chapter 3 describes the experimental details, including sample preparation by Sol-gel methods and equipment setups. We will give the results and discussions about $\text{Pb}_x\text{La}_{1-x}\text{TiO}_3$ systems including phase transitions and LO-TO splitting and the dominant mechanism on green emission of Er^{+3} -doped $\text{Pb}_{0.8}\text{La}_{0.2}\text{TiO}_3$ thin film in Chap 4. In the final Chapter, we conclude the investigations on the $\text{Pb}_x\text{La}_{1-x}\text{TiO}_3$ thin film and proposed several topics worthy of further studying.

Chapter 2

Theoretical Background

2.1 X-ray diffraction

Fig. 2-1 illustrates for the particular condition described the only diffracted beam form is that shown, namely one making an angle of reflection θ equal to the angle of incident θ . We will show this, first, for one plane of atoms and, second, for all the atoms making up the crystal. Consider rays **1** and **1a** of the incident beam, they strike atoms *K* and *P* on the first plane of the crystal and are scattered in all directions. While in the directions **1'** and **1a'** of the scattered beams are completely in phase capable of reinforcing each other; because the path difference between the wave fronts **XX'** and **YY'** is equal

$$QK - PR = PK \cos \theta - PK \sin \theta = 0, \quad (2.1)$$

Similarly, the scattered rays from all the atoms on the first plane to the directions parallel to **1'** are in phase contribute to the diffracted beam. This will be true for all of the planes, and it remains to find the condition of rays scattered by atoms on the different planes. Consider parallel lattice planes spaced d' apart. Ray **1** and **2**, for example, are scattered by atoms *K* and *L*, and the path difference of the rays **1KI'** and **2L2'**,

$$ML + LN = d' \sin \theta + d' \sin \theta, \quad (2.2)$$

is equal to the path difference of the overlapping rays scattered by *S* and *P* in the same direction shown in Fig. 2.1, since in this direction there is no path difference between rays scattered by *S* and *L* or *P* and *K*. The scattered rays **1'** and **2'** will be completely in phase if the path difference is equal to an integer number n of wavelengths λ , i.e.,

$$n \lambda = 2d' \sin \theta . \tag{2.3}$$

This relation was first formulated by Bragg and is known as the Bragg's law. Assuming $n = 1$, we can consider a reflection of any order as a first-order reflection from planes, real or fictitious, spaced at a distance $1/n$ of the previous spacing. This turns out to be a real convenience, so we set $d = d'/n$ and write the Bragg law in the form $\lambda = 2d \sin \theta$.

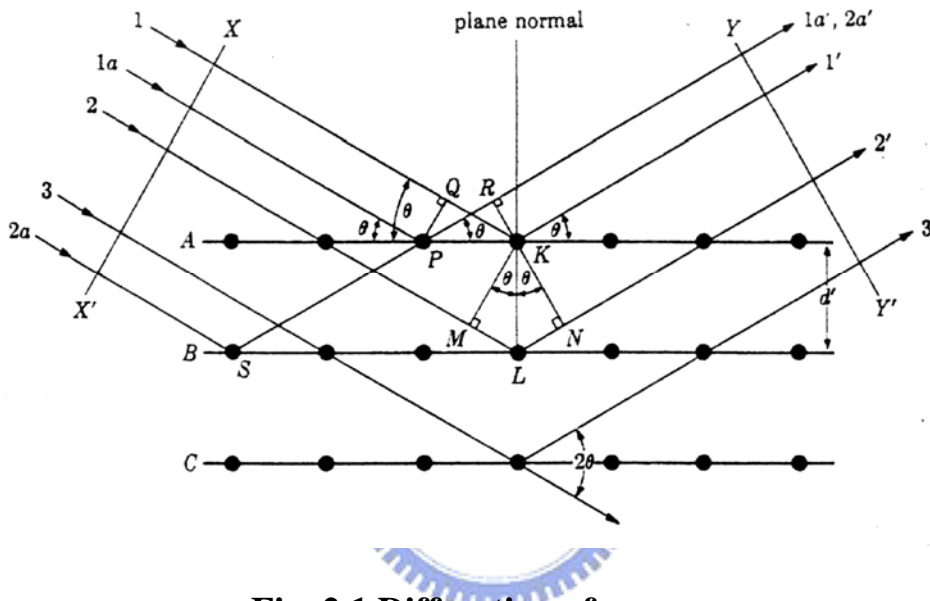


Fig. 2.1 Diffraction of x-ray

What determine the possible directions, referring to Fig. 2.2, we see that various diffraction angles $2\theta_1, 2\theta_2, 2\theta_3, \dots$ can be obtained from the (100) plane by using a beam incident at the correct angle $\theta_1, \theta_2, \theta_3, \dots$ and producing first-, second-, third-, ... order reflections. But diffraction can also be produced by the (110) planes, the (111) planes, the (213) planes, and so on. We obviously need a general relation which predicts the diffraction angle for any set of planes. This relation is obtained by combing the Bragg law and the plane-spacing equation.

For example, The value of d , the distance between adjacent planes in the set

(*hkl*), if the crystal is cubic, then

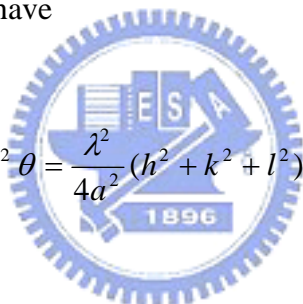
$$\lambda = 2d \sin \theta \quad (2.4)$$

and

$$\frac{1}{d^2} = \frac{(h^2 + k^2 + l^2)}{a^2}, \quad (2.5)$$

where *a* is the lattice constant.

Combing these equations, we have


$$\sin^2 \theta = \frac{\lambda^2}{4a^2} (h^2 + k^2 + l^2). \quad (2.6)$$

This equation predicts, for a particular incident wavelength λ and a particular cubic of the unit cell size *a*, all the possible Bragg angle at which diffraction can occur from the planes (*hkl*). For (110) planes, for example, Eq. (2-6) becomes $\sin^2 \theta_{110} = \frac{\lambda^2}{2a^2}$

If the crystal is tetragonal, with axes *a* and *c*, then the corresponding general equation is

$$\sin^2 \theta = \frac{\lambda^2}{4} \left(\frac{h^2 + k^2}{a^2} + \frac{l^2}{c^2} \right) \quad (2.7)$$

and similar equations can readily be obtained for the other crystal systems.

These examples show that the directions, in which a beam of given wavelength is diffracted by a given set of lattice planes, are determined by the crystal system to which the crystal belongs to and its lattice parameters. In short, diffraction directions are determined solely by the shape and size of the unit cell. This is an important point and so is its converse: all we can possibly learn about an unknown crystal by measurements of the directions of diffracted beams are the shape and size of the unit cell.

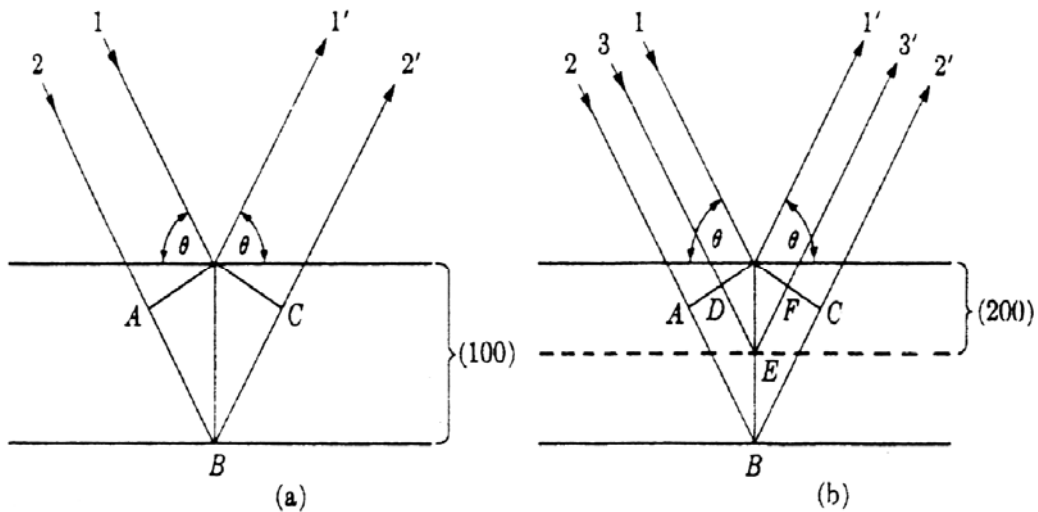


Fig 2-2 Equivalence of (a) a second-order 100 reflection and (b) a first-order 200 reflection.

2.2 Phonon modes of ABO₃-type perovskite

2.2.1 IR absorption

For infra-red (IR) wavelengths, absorption must in some way be related to a variation in the charge distribution. This arises due to a change in the dipole moment associated with molecule. After bonding, one atom of the molecules has a local charge Δq then the rest of atoms have charge $-\Delta q$ and the dipole moment μ , is given by

$$\mu = \Delta q \times l \quad (2-8)$$

where l is the separation of the charges (see Fig. 2.3).

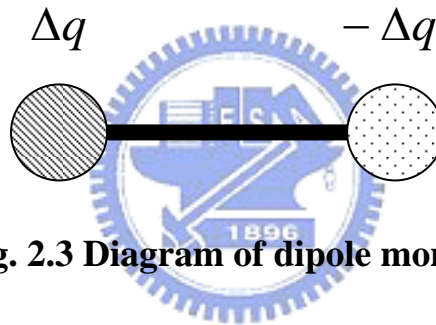


Fig. 2.3 Diagram of dipole moment

Electromagnetic wave can be absorbed or emitted by a medium if during its interaction there is a change in the charge distribution within the medium. During the interaction with photon, the dipole moment μ will change, thus can rewrite the dipole moment as

$$\mu = \mu_0 + \frac{\partial \mu}{\partial Q} Q \quad (2.9)$$

where $Q = (r - r_{eqm})$ is the displacement from the equilibrium positions r_{eqm} .

In order to describe the excitation of a molecule from vibrational level $\nu = i$ to $\nu = f$ as shown in Fig. 2.4. The total Hamiltonian is described, an interaction Hamiltonian $H_{int} = E \cdot \mu$ that expresses the interaction of an atom with a photon, to the unperturbed Hamiltonian H_0 , as $H = H_0 + H_{int}$ (2.11)

Thus the transition moment, R can be written as

$$R = \int \psi_i H_{\text{int}} \psi_f = \langle i | H_{\text{int}} | f \rangle \quad (2.12)$$

so,

$$R = \langle i | \left(\mu_0 + Q \frac{\partial \mu}{\partial Q} \right) \cdot E | f \rangle = \langle i | \frac{\partial \mu}{\partial Q} \cdot E | f \rangle \quad (2.13)$$

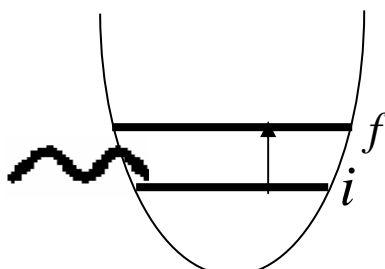


Fig. 2.4 Transition from level i to f

IR absorption occurs as the transition $R \neq 0$, in other words there must be a change in the dipole moment due to vibration of the molecule which is induced by the applied field E , since the transition probability P is equal to R^2 . The condition that an IR absorption, or emission must be associated with a change in dipole moment is known as the dipole selection rule. The dipole selection rule plays an important role in IR spectroscopy because it tells us whether a molecule will be IR active or not.

2.2.2 Raman scattering

When light passes through a medium, most of the light is reflected, transmitted, absorbed, elastic scattered, or inelastic scattered. Raman scattering is an inelastic scattering process. When the light encounters the medium, it interacts inelastically with phonon modes and produces outgoing photons whose frequencies are relatively shifted by an amount of energy correspondent to phonon energy from that of the incoming light. The scattered outgoing photons are called the Raman-scattered photons. If the light of frequency ν_0 is scattered by some media, the spectrum of the scattered light contains a strong line of frequency ν_0 and much weaker lines of frequencies $\nu_0 - \Delta\nu_1$, $\nu_0 - \Delta\nu_2$,, $\nu_0 + \Delta\nu_2$, $\nu_0 + \Delta\nu_1$, etc. Those lines on the low frequency side of the exciting lines (i.e. $\nu_0 - \Delta\nu_i$, $i = 1, 2, \dots$) are always matched

by lines on the high frequency side (i.e. $\nu_0 + \Delta\nu_i, i = 1, 2, \dots$) but the latter are much weaker when the scattering medium is at room temperature. Raman scattering is inherently a weak process, but laser provides enough intensity that the spectra can be routinely measured. In analogy with terms used in the discussion of fluorescence spectra, lines on the low frequency side of the exciting line are known as Stokes lines and those on the high frequency side as anti-Stokes lines.

The incident photon loses its energy by producing a phonon (Stokes shifted), or gain energy and momentum by absorbing a phonon (anti-stokes shifted), according to the energy and momentum conservation rules :

$$h\nu_s = h\nu_i \pm h\Omega \quad (2.14)$$

$$q_s = q_i \pm K \quad (2.15)$$

where ν_i and ν_s are the incoming and scattered photon frequencies, q_i and q_s are the incoming and scattered photon wavevectors, Ω and K are the phonon frequency and wavevector, respectively.

All the Raman mode frequencies, intensities, line-shape, and line-width, as well as polarization behavior can be used to characterize the lattice and impurities. The intensity gives information on crystallinity. The line-width increases when a material is damaged or disordered, because damage or disorder occurs in a material will increase phonon damping rate or relax the rules for momentum conservation in Raman process. All these capabilities can be used as a judgment for layered microstructure as well as bulk materials, subject only to the limitation that the penetration depth of the exciting radiation range from a few hundred nanometers to few micrometers.

2.3 Mechanism of LO-TO splitting

The total polarization in the crystal can be expressed as a sum of contributions from the displacements of the charged ions and from the displacements of electrons

relative to their ionic nuclei

$$P^i = P_{ion}^i + P_{electron} \quad (2.16)$$

and

$$P_{ion}^i = \frac{N}{V} \sum_{\alpha} e_{\alpha} U_{\alpha}^i \quad (2.17)$$

where i is the label of Cartesian coordinate, N is the number of primitive cells in the crystal volume V and e_{α} is the charge of the α th ions in a primitive cell, all ions of the same label suffering the same displacement U_{α} .

It is convenient to express the ionic polarization in terms of the normal coordinates. The polarization is a vector, and the vibrational modes that contribute to the polarization are limited to those with the same symmetry character as a polar vector. These polar modes can be chosen so that their contributions to the polarization are parallel to principal axes of the susceptibility tensor. Let ξ_{σ} be a unit vector parallel to the polarization contributed by the displacement of normal coordinates W_{σ} .

Then one of the Cartesian components ξ_{σ}^i is unity and the other two are zero. The ionic polarization can be written as

$$P_{ion}^i = \frac{N}{V} \sum_{\sigma} Z_{\sigma} \xi_{\sigma}^i W_{\sigma}, \quad (2.18)$$

$$Z_{\sigma} \xi_{\sigma}^i \equiv \sum_{\alpha} \frac{e_{\alpha} c_{\alpha\sigma}^{i*}}{M_{\alpha}^{1/2}}, \quad (2.19)$$

where Z_{σ} is the effective charge of the normal mode σ and the mass of the α th atom is denoted by M_{α} . By the simplification equations of motion, we obtain

$$W_{\sigma} = \sum_{\alpha} W_{\alpha}^{1/2} c_{\alpha\sigma}^i U_{\alpha}^i, \quad (2.20)$$

where the transformation coefficients can be chosen to satisfy the orthonormality relations

$$\sum_{\alpha} c_{\alpha\sigma}^{i*} c_{\alpha\sigma'}^i = \delta_{\sigma\sigma'}. \quad (2.21)$$

The presence of an electric field E modifies the harmonic oscillator equation of the normal mode to

$$\ddot{W}_{\sigma} + \Gamma_{\sigma} \dot{W}_{\sigma} + \omega_{\sigma}^2 W_{\sigma} = Z_{\sigma} \xi_{\sigma}^i E^i. \quad (2.22)$$

The applied electric field of frequency ω , therefore, produces a steady-state

normal-mode amplitude,

$$W_\sigma = \frac{Z_\sigma \xi_\sigma^i E^i}{\omega_\sigma^2 - \omega^2 - i\omega\Gamma_\sigma} \quad (2.23)$$

and the ionic polarization can be written in a form proportional to the electric-field components. We assume that ω is in the vicinity of the vibrational frequencies and well below the frequencies of all electric transitions. The relative permittivity is then

$$\kappa^i = \kappa_\infty^i + \sum_\sigma \frac{NZ_\sigma^2 \xi_\sigma^{i2} / \varepsilon_0 V}{\omega_\sigma^2 - \omega^2 - i\omega\Gamma_\sigma}, \quad (2.24)$$

where κ_∞^i is a constant electric contribution to the relative permittivity, so that

$$P_{electron}^i = \varepsilon_0 (\kappa_\infty^i - 1) E^i. \quad (2.25)$$

The electric field and polarization of any electromagnetic wave frequency ω and wavevector q will satisfy the Maxwell's equations :

$$-\varepsilon_0 c^2 q(q \cdot E) + \varepsilon_0 (c^2 q^2 - \omega^2) E = \omega^2 P, \quad (2.26)$$

This equation is unfortunately very complicated in its most general form, but simplification can be made for most applications. The most striking simplification occurs when the frequency and wavevector satisfy $cq \gg \omega$. We obtained

$$\kappa^x q^x q^2 + \kappa^y q^y q^2 + \kappa^z q^z q^2 = 0 \quad (2.27)$$

By combining the equation for the divergence of the electrical displacement

$$q \cdot (\varepsilon_0 E + P) = 0, \quad (2.28)$$

and Eqs. (2.26) and (2.27) two equations above, we can obtain the general representation

$$\ddot{W}_\sigma + \omega_\sigma W_\sigma = - \frac{NZ_\sigma (q \cdot \xi_\sigma) \sum_\tau Z_\tau (q \cdot \xi_\tau) W_\tau}{\varepsilon_0 V (\kappa_\infty^x q^x q^2 + \kappa_\infty^y q^y q^2 + \kappa_\infty^z q^z q^2)}, \quad (2.29)$$

where τ is summed over all the polar modes. In cubic symmetry crystal, the polar-vector representation is threefold degenerate. The crystals are optically isotropic and the principal axes are not restricted to lie in any particular directions. For any direction of the wavevector of a threefold polar mode, it is permissible to choose two of the polarization vectors ξ_σ perpendicular to q and the third ξ_σ parallel to q . The two transverse polar modes have a frequency determined by the standard lattice dynamics calculation. The longitudinal polar mode has the associated macroscopic electric field, and its frequency is determined by the equation above, which reduces to

$$\kappa = 0 \quad (2.30)$$

in the cubic case. The simplest cases to consider first are the cubic crystals that have a single threefold polar mode. The relative permittivity has the isotropic form

$$\kappa = \kappa_\infty + \frac{NZ^2 / \varepsilon_0 V}{\omega_T^2 - \omega^2 - i\omega\Gamma}, \quad (2.31)$$

where the mode frequency ω_0 is replaced by ω_T to emphasize its transverse nature and redundant subscripts and superscripts are omitted. The longitudinal frequency obtained from the equation mentioned above with the damping removed is

$$\omega_L = \left(\frac{\kappa_0}{\kappa_\infty}\right)^{1/2} \omega_T, \quad (2.32)$$

where κ_0 is the zero-frequency value of the relative permittivity

$$\kappa_0 = \kappa_\infty + \frac{NZ^2}{\varepsilon_0 V \omega_T^2}. \quad (2.24)$$

This expression for the longitudinal frequency is the Lyddane-Sachs-Teller relation. The equation of motion for the longitudinal mode takes the form

$$\ddot{W} + \omega_T^2 W = -\frac{NZ^2 W}{\varepsilon_0 V \kappa_\infty}, \quad (2.25)$$

and leading to

$$\omega_L^2 = \omega_T^2 + \frac{NZ^2}{\varepsilon_0 V \kappa_\infty}. \quad (2.26)$$

Resta *et al.* [16] have shown that polarization is linear in the change of the position vector of the basis atom to a good approximation. The Born effective charge tensor Z_m^* is rewritten through

$$\delta P = \frac{e}{\Omega} \sum_{m=1}^N Z_m^* \cdot \delta u_m \quad (2.27)$$

Here, N is the number of atoms in the primitive unit cell, δu_m is the first-order change of the position vector of the m th basis atom, and Ω is the volume of the unit cell.

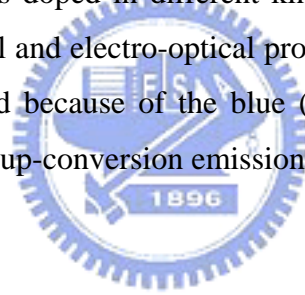
The Born effective charge tensor reflects the effects of the Coulomb interactions and is directly related to the LO-TO splitting. The general representation of the dynamical material for LO and TO modes at $q=0$ are related by

$$D_{mn}^{LO} = D_{mn}^{TO} + \frac{4\pi e^2}{\Omega} \frac{Z_m^* Z_n^*}{\epsilon_0} \quad (2.28)$$

where D represents the dynamical matrix and is proportional to the square of the vibration frequency. Zhong *et al.*[11] and Waghmare *et al* [17] have calculated that the softest TO mode is most associated with the hardest LO mode via Coulomb interaction to give rise to giant LO-TO splitting in ABO_3 compounds, especially for the ferroelectric phonon modes.

2.4 Emission spectrum of energy levels of Er^{3+} -doped thin film

Rare-earth ions exhibit a characteristic intra-4f shell luminescence which is nearly both host material and temperature independent [6]. This feature can be used to tune the emission spectra for specific applications. Thus, it is important for systematic research of the rare-earth ions doped in different kinds of host materials with good mechanical, thermal, electrical and electro-optical properties. Erbium-doped materials have been extensively studied because of the blue (${}^2H_{9/2} \rightarrow {}^4I_{15/2}$), green (${}^4S_{3/2}, {}^2H_{11/2} \rightarrow {}^4I_{15/2}$) and red (${}^4F_{9/2} \rightarrow {}^4I_{15/2}$) up-conversion emissions. (see Fig. 2.5)



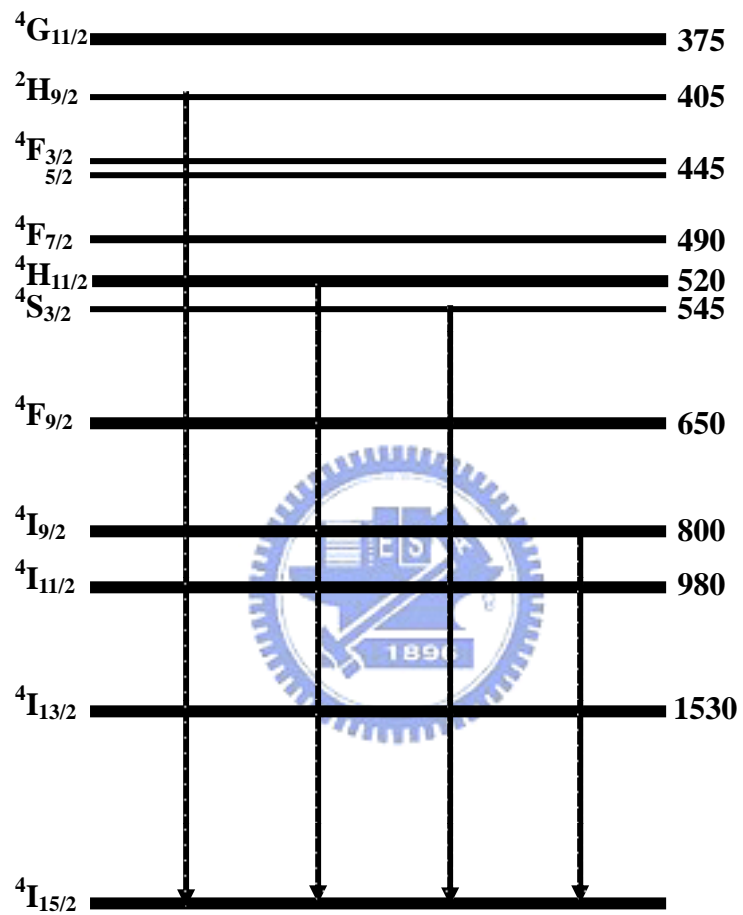


Fig. 2.5 $4f$ energy levels in the PL of PLT:Er⁺³ thin films.

Chapter 3

Experimental detail

3.1 Sample preparation

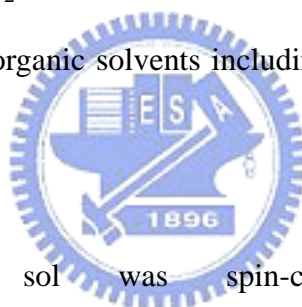
The sol-gel technique was adopted to prepare $Pb_{1-x}La_xTiO_3$ and Er-doped $Pb_{0.80}La_{0.20}TiO_3$ thin films to yield homogeneous samples with highly accurate composition. We will describe in detail the procedure of sol-gel methods as follows.

3.1.1 Thin film preparation

In order to prepare the $Pb_{1-x}La_xTiO_3$ thin films (PLT) by the sol-gel technique in the range of $x=0.00$ to 0.30 , ($x=0, 0.05, 0.10, \dots, 0.7$), the quantity (in gram) of precursors of Pb and La are listed in Table 3.1 and that of Er doped $Pb_{0.8}La_{0.2}TiO_3$ is listed in Table 3.2. Shown in Fig. 3.1 [(1)~(6)] and Fig. 3.2 [(7)~(11)] are the flow charts of sol-gel procedure for preparing PLT and Er doped PLT solution, respectively.

- (1) 2-Methoxyethanol(2-MOE) 20ml was heated up to $120^\circ C$ for 5 min.
- (2) A proper amount of lead acetate, Lanthanum acetate and Erbium acetate according to Table 3.1 and Table 3.2 was co-dissolved in 2-Methoxyethanol and stirred for 30 min.
- (3) Nitric Acid was added as to catalysis for helping completely hydrolyze the precursors.

- (4) A proper amount of Titanium isopropoxide was dissolved in 2-Methoxyethanol and the solution was poured into Pb-La compound solution at 90°C , while stirring continuously for approximately 30 min.
- (5) Formamide was added to adjust the viscosity of PLT sol. The PLT sol is clear and transparent.
- (6) For preparing coating agent, the parent sol was diluted to 0.3 M with 2-Methoxyethanol.
- (7) The Pt(100nm)/TiO₂/SiO₂/Si substrates were cleaned by ultrasonication thoroughly in a series of organic solvents including Acetone(ACE) and Isotropic Alcohol(IPA).
- (8) The diluted PLT sol was spin-coated on the cleaned Pt(100nm)/TiO₂(50nm)/SiO₂/Si substrates at $800\text{ rev}\cdot\text{min}^{-1}$ for 20sec and then $3500\text{ rev}\cdot\text{min}^{-1}$ for 40sec.
- (9) After each spin coating, the substrates were heated at 200°C in ambient atmosphere for 10 min to dry the gel.
- (10) To accumulate the film thickness, the film was coated and heated at 200°C 10~20 times.
- (11) Finally, the samples were sintered at different temperatures for one hour.

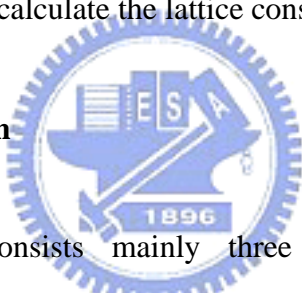


3.2 Characterization

3.2.1 X-ray diffraction system

The study of the samples in the PLT system was accomplished using X-ray powder diffraction (XRD) in Shimadzu XD-5 diffractometer and monochromatic in high intensity Cu-k α line of wavelength 1.5405Å. Data were recorded between the angle range $20^\circ < 2\theta < 60^\circ$ with steps of 0.04° . The maximum voltage of the system is 30 kV, with the maximum current 20 mA and rate of scanning is $4^\circ/\text{min}$. The resulting XRD patterns were Gaussian fitted to get the diffraction peaks and widths. By comparing with the JCPDS data, the fitted peaks positions and corresponding reflection planes were used to calculate the lattice constants.

3.2.2 Raman detection system



Raman spectroscopy consists mainly three components : laser system, spectrometer, and computer. Fig. 3.3 shows schematics of experimental setup. An-ion laser (Coherent INNOVA 90) provides an excitation source of a wavelength 488nm. The unwanted plasma lines were filtered out by a laser-line filter. A biconvex spherical lens with a focal length of 5cm was used to focus the laser beam onto the sample surface at 45 degree reflection geometry. The laser power on the sample surface is about 30~50 mW with beam spot size of 30~50 μm (in diameter). The scattered light was collected by a camera lens and imaged onto the entrance slit of a spectrograph (Spex triplemate1877C) which is equipped with a liquid-nitrogen cooled charge coupled device (CCD) detector array (Phometrics CC200).

3.2.3 PL measurement system

Photoluminescence (PL) of Er-doped $\text{Pb}_{0.8}\text{La}_{0.2}\text{TiO}_3$ thin films were carried out by pumping with the 488 nm line of Ar^+ laser. The wavelength of the emission photon is observed in 510 nm to 680 nm. The experimental setup is the same as that described in Raman measurement.(see Fig. 3-3)



Pharmaceuticals Ratio(Pb : La)	Pb(CH₃COO)₂.3H₂O (g)	La(CH₃COO)₃(g)
1.00 : 0.00	2.276040	0
0.95 : 0.05	2.162238	0.102918
0.90 : 0.10	2.048436	0.205836
0.85 : 0.15	1.934634	0.308754
0.80 : 0.20	1.820832	0.411672
0.75 : 0.25	1.707030	0.514590
0.70 : 0.30	1.593228	0.617508

Table 3-2 The components ratio of Pb-La

Pharmaceuticals Er⁺³ concentration	Pb(CH₃COO)₂.3H₂O(g)	La(CH₃COO)₃ (g)	Er(CH₃COO)₃(g)
1 mol%	1.80262	0.40756	0.02066
3 mol%	1.76620	0.39930	0.06198
5mole%	1.72980	0.39108	0.10330

Table 3-2 The components ratio of Pb-La-Er

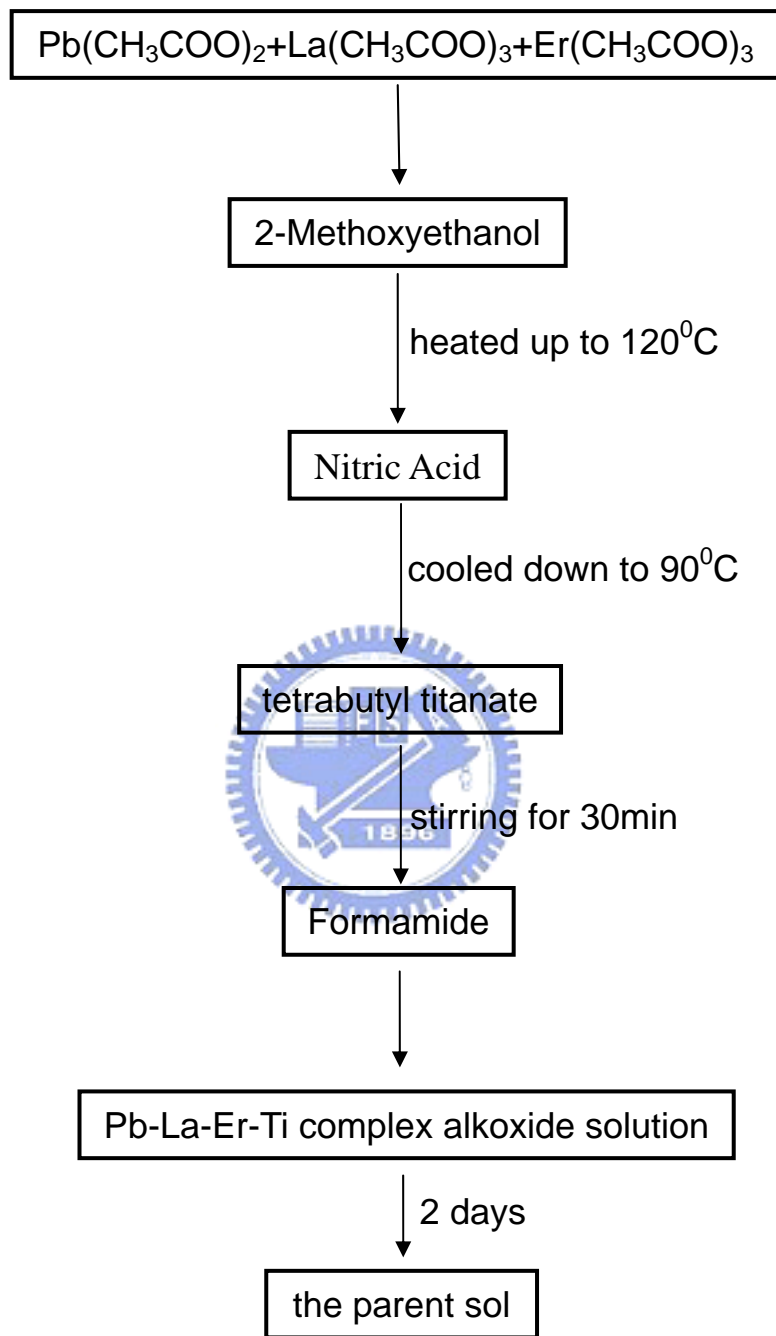


Fig. 3.1 Flowchart of Er-doped PLT solution obtained by sol-gel method

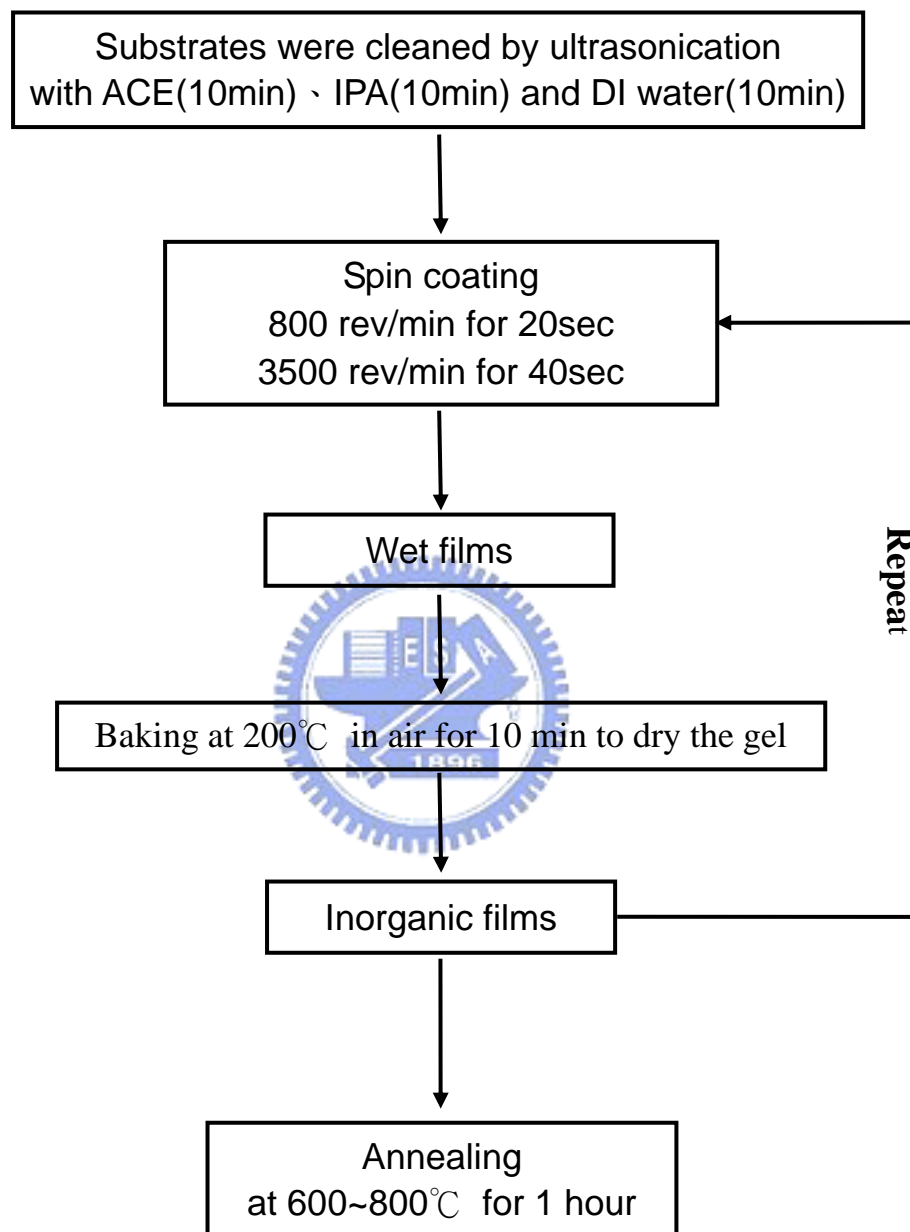


Fig. 3.2 Flowchart of sol-gel derived Er-doped PLT thin films

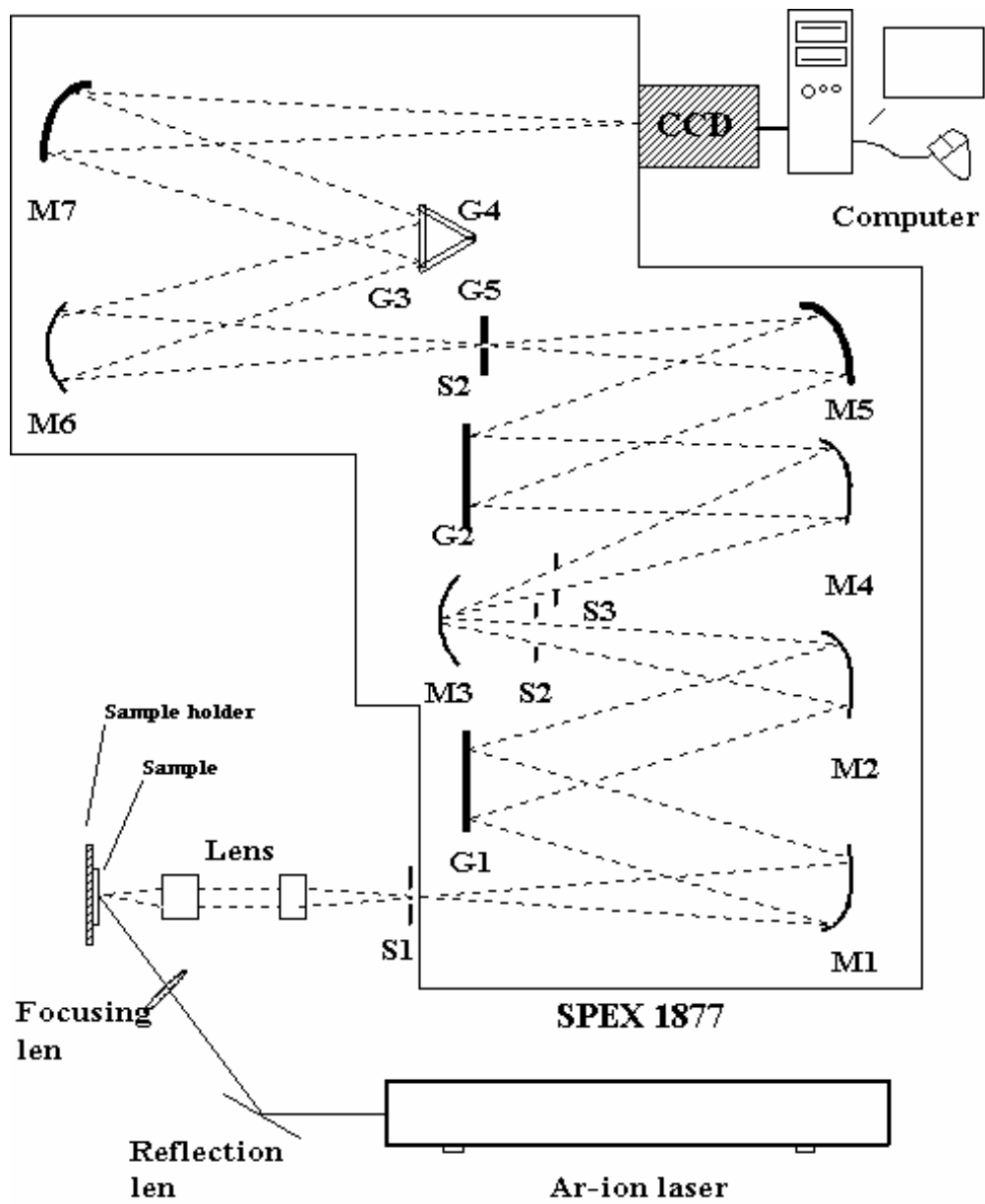


Fig. 3.3 Setup of Raman and visible-PL measurement.

Chapter 4

Results and Discussions

4.1 Results of the $\text{Pb}_{1-x}\text{La}_x\text{TiO}_3$ (PLT) thin films

4.1.1 Results of the X-ray diffraction

Fig. 4.1 shows X-ray diffraction (XRD) patterns of samples with various x values, obtained by the aforementioned sol-gel processes. The lattices parameters of the samples were measured at room temperature as a function of x from 0.00 to 0.70. The splitting of (100) and (001) diffraction peaks indicates the tetragonal crystal structure of the film. With lanthanum addition the splitting becomes less evident and the doublets tend to merge into a single peak. Fig 4.2 shows the plot of the full width at half maximum (FWHM) of the (101) diffraction peak with lanthanum doping. The FWHM of $\text{Pb}_{1-x}\text{La}_x\text{TiO}_3$ thin films decreased obviously down to $x=0.20\sim 0.25$. The diminution of the FWHM of the $\text{Pb}_{1-x}\text{La}_x\text{TiO}_3$ thin films could be due to an increase in crystallinity. That indicates that the $\text{Pb}_{1-x}\text{La}_x\text{TiO}_3$ thin films have the best crystallinity at $x=0.20\sim 0.25$.

The resulting XRD patterns were analyzed from 2.1. We used the tetragonal for all PLT compounds to obtain the lattice constants of a-axis and c-axis. Fig. 4.3(a) shows the x-dependence of the lattice constants and Fig. 4.3(b) plots the x-dependence of the tetragonality, c/a . The figure shows that the tetragonality declines from 1.044 to 1.000 as x changes from 0.00 to 0.25, corresponding to the tetragonal-cubic phase transition.

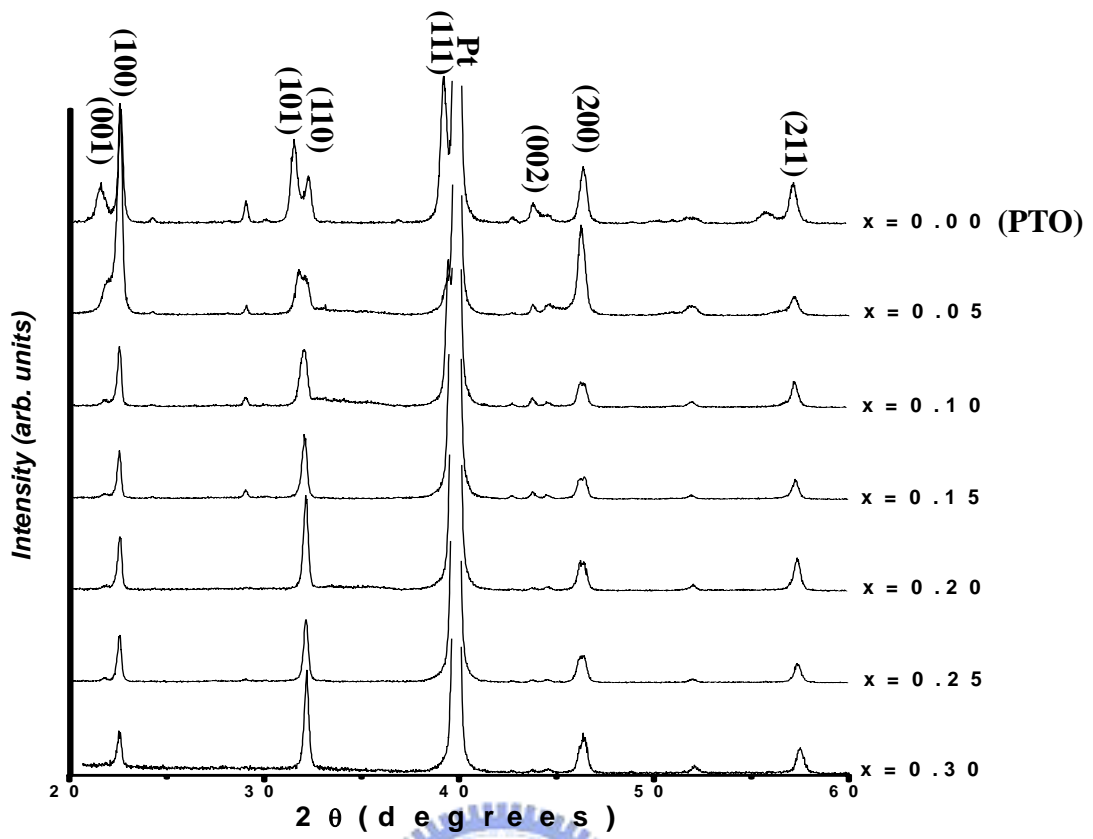


Fig. 4.1 XRD patterns of $\text{Pb}_{1-x}\text{La}_x\text{TiO}_3$ samples with various x values

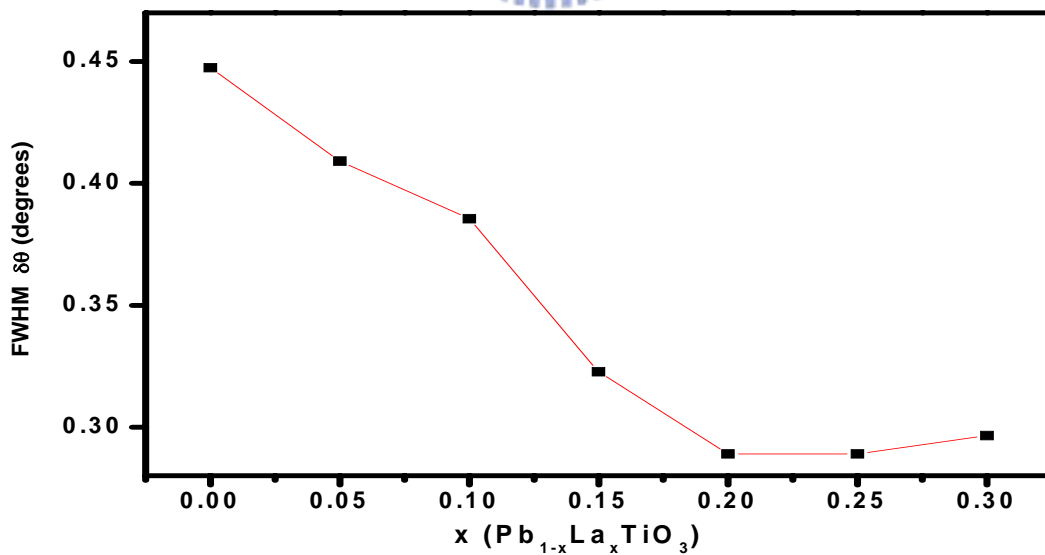


Fig.4.2 The variation of the FWHM of the (101) peak of $\text{Pb}_x\text{La}_{1-x}\text{TiO}_3$

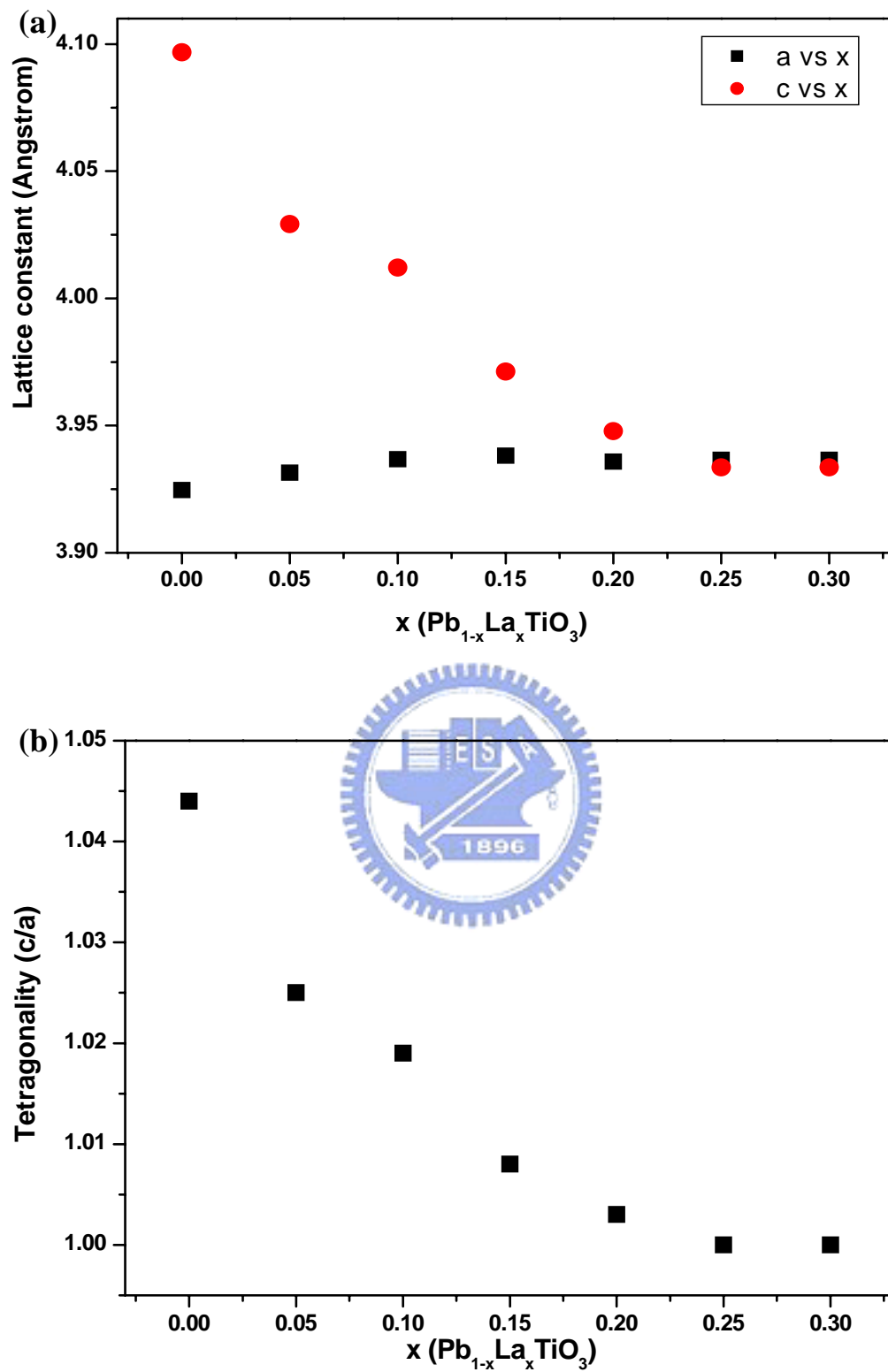


Fig. 4.3 (a) Lattice constant “a” and “c” (b) c/a ratio of Pb_xLa_{1-x}TiO₃

4.1.2 Analysis of the Raman spectra

PbTiO₃ belongs to the O_h¹ (*Pm3m*) space group, with one formula unit per primitive cell, in the cubic (paraelectric) phase. Thus there are 12 optic modes at the Γ point of the Brillouin zone. The optic modes transform the 3T_{1u}+T_{2u} irreducible representation of the O_h point group. The T_{1u} modes are infrared active and T_{2u} is the so-called “silent mode” since it is neither infrared nor Raman active. In the ferroelectric tetragonal phase [C_{4v}¹ (*P4mm*) space group] each triply degenerate T_{1u} mode splits into two modes transforming as the A₁+E irreducible representation of the C_{4v} point group. The silent mode also, in principle, splits into B₁+E mode that are Raman active; however, the separation between these two modes cannot be measured, so that the single feature that one measures for these phonons is called B₁+E. We follow the straightforward labeling scheme used earlier, and ignoring the B₁+E feature, the following modes should be observable in the tetragonal ferroelectric phase in Table 4-1.

Mode	Reference 30	This work
E (1TO)	80	83
A ₁ (1TO)	116	120
E(1LO)		145
E(2TO)	206	205
B ₁ +E		286
A ₁ (2TO)	341	337
E(2LO)+ A ₁ (2LO)	443	440
E(3TO)	501	501
A ₁ (3TO)	620	613
E(3LO)	720	695
A ₁ (3LO)	720	758

Table 4.1: Frequencies (in cm⁻¹) of observed Raman lines in the PbTiO₃ films at room temperature

Fig. 4.4 displays the Raman spectra of $\text{Pb}_{1-x}\text{La}_x\text{TiO}_3$ thin films taken at room temperature for various x values. Lorentzian line fitting was adopted to decompose the overlapping modes.[18] For pure PbTiO_3 , Fig. 4.5(a) shows the fitting results are not in good agreement with experimental spectra. The intensities of the fitting data are weaker than those of the experimental spectra at 173cm^{-1} and 250cm^{-1} and the fitting result of the $A_1(3\text{TO})$ mode is also not good at 613cm^{-1} . Considering disorder-induced background, Fig. 4.5(b) shows the fitting results are in good agreement with experimental spectra. In Fig. 4.6, the intensity of disorder induced background contrast to that of phonon mode becomes strong while x increases. It means that the disorder induced background is obvious at cubic phase.

The Raman spectra of PbTiO_3 (PTO) thin films deposited on $\text{Pt}/\text{TiO}_2/\text{SiO}_2/\text{Si}$ substrates with different thickness was shown in Fig. 4.7. As can be seen, the frequency of soft mode $E(1\text{TO})$ of the film coated 10 times (82.70cm^{-1}) is close to that of the film coated 20 times (83.10cm^{-1}). It indicates that the influence of stress exists in the films due to lattice mismatch between the film and substrate is slight. It means that the films coated 20 times are thick enough to ignore the influence of stress in this work.

Fig. 4.8 shows, the x -dependent phonon modes are assigned following Foster *et al*[23], to clarify the structural variation of the $\text{Pb}_{1-x}\text{La}_x\text{TiO}_3$ system. Fig. 4.8 shows that a tetragonal to cubic phase transition was found at composition $x=0.20\sim 0.25$ of the $\text{Pb}_{1-x}\text{La}_x\text{TiO}_3$ system detected by Raman spectroscopy. It coincides with XRD measurement. Undergoing the tetragonal to cubic phase transition, unlike the analysis of S. Y. Kuo *et al*[13], $A_1(3\text{TO})$ phonon mode and $E(3\text{TO})$ phonon mode would approach, but not merge into a single whole in this work while we consider disorder-induced background. The intensities of those become weak and the FWHM become broad. It is reasonable. For the cubic phase, the influence of Ti-disorder on

the A_1 phonon mode and E phonon mode is different. Consequently the A_1 phonon mode and E phonon mode due to the influence of Ti-disorder are not inseparable.

The variation of the soft mode E(1TO), which corresponds to vibration of the Pb ion with respect to the slightly distorted TiO_6 octahedra. This soft mode is very sensitive to the pressure [19], temperature [20] and substitution of Pb or Ti by other elements [21-22]. The first two factors can be excluded in the present case because measurements were carried out at room temperature in 1 atmosphere. According to Fig. 4.4, the lowest TO phonon modes are found to be ‘softened’ and the FWHM of the peak increase while x increase from 0.00 upward 0.10.

Following the calculation of Born effective charges of ABO_3 pervoskites by Zhong *et al.*[11] and Waghmare *et al* [17], we comprehend that the calculated mode effective charge for the softest TO mode is the largest as listed in Table III and Table IV of [11] and [17], respectively. It means that the soft mode will couple strongly with the crystal field. Due to strong mode mixing via coulomb interaction, the softest TO [A_1 (1TO)] mode is most closely associated with the hardest LO [A_1 (3LO)] mode that gives rise to a giant LO-TO splitting behavior which is dominated by

$$D_{mn}^{LO} = D_{mn}^{TO} + \frac{4\pi e^2}{\Omega} \frac{Z_m^* Z_n^*}{\epsilon_0}, \quad (5.1)$$

where D represents the dynamical matrix and is proportional to the square of the vibration frequency; Ω is the volume of the unit cell, and Z^* is the Born effective charge. Fig. 4.9 shows the difference between the square of A_1 (3LO) and A_1 (1TO) phonon frequencies for PST powders[13] and PLT thin film. They have the same tendency. The decreased splitting phenomenon observed is ascribed to that Pb-O interaction is hybridized, and thus the change of effective charge to the LO-TO splitting is the dominant mechanism.

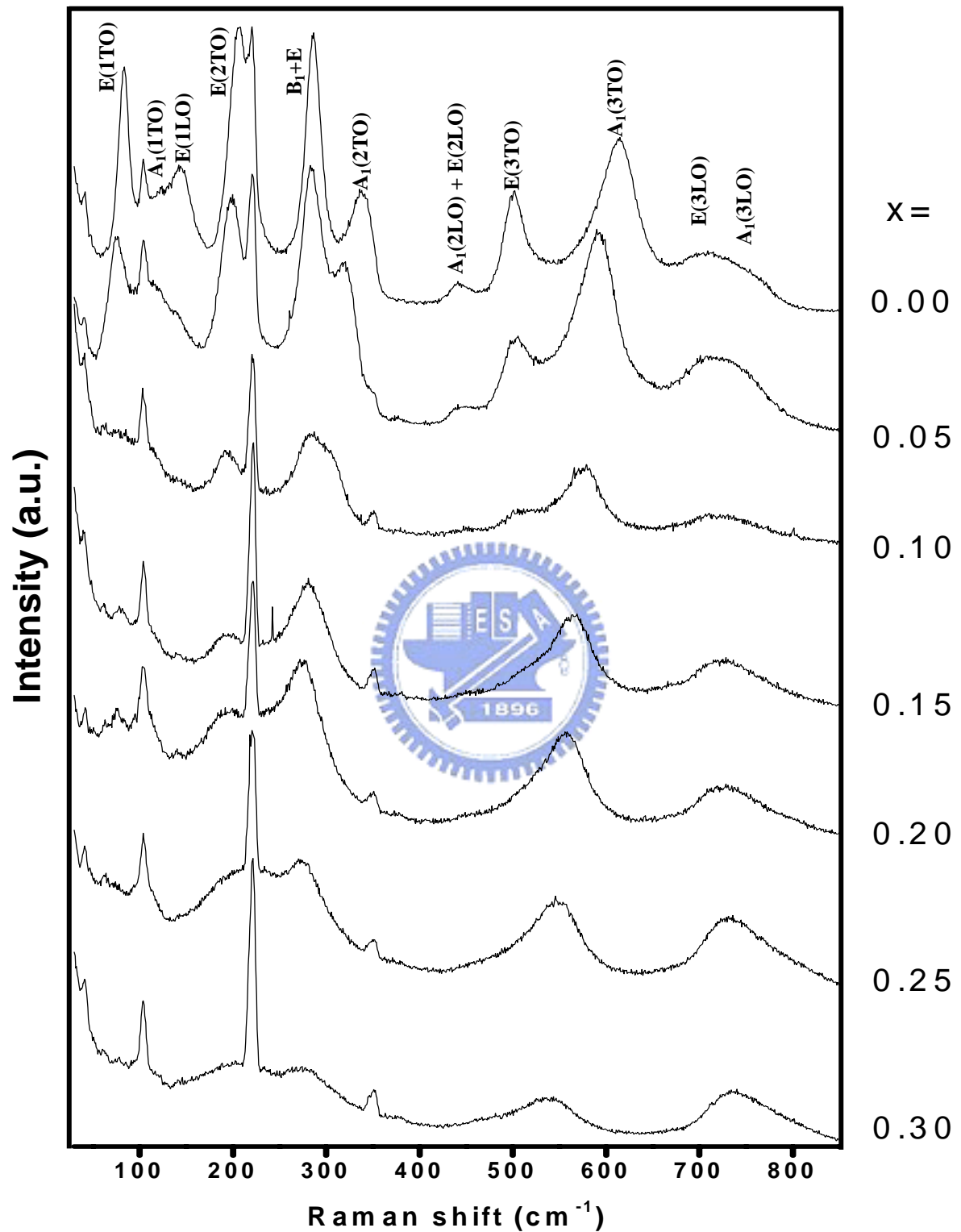
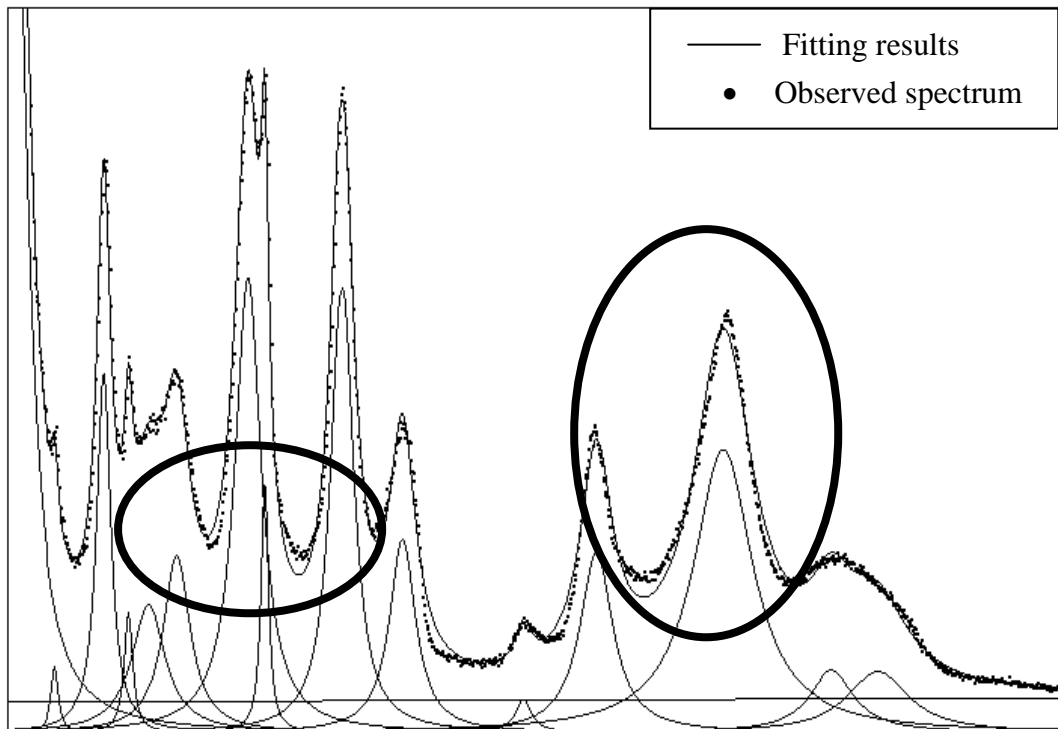


Fig. 4.4 Raman spectra of $\text{Pb}_{1-x}\text{La}_x\text{TiO}_3$ thin films at room temperature

(a) **PbTiO₃ thin film**



(b)

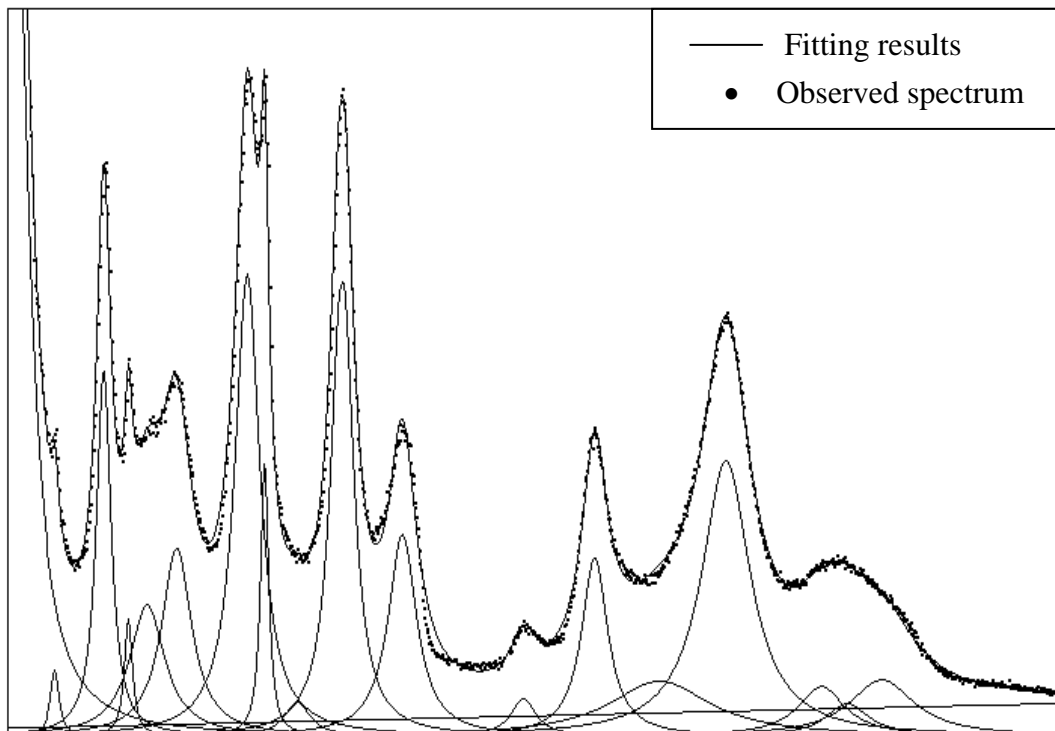


Fig. 4.5 (a) A bad fitting results (b) A well fitting results compared with the experiment spectrum

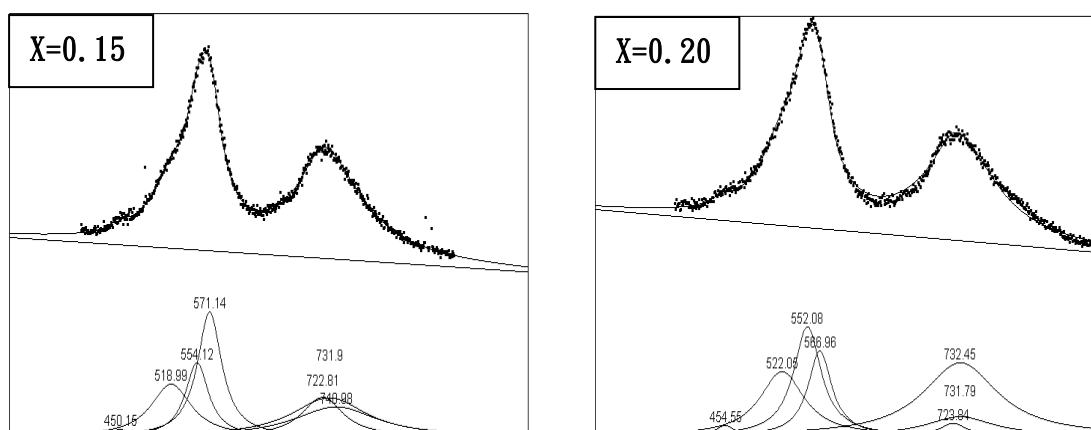


Fig. 4.6 The intensity of disorder induced background of $\text{Pb}_{1-x}\text{La}_x\text{TiO}_3$ sample with different La concentrations

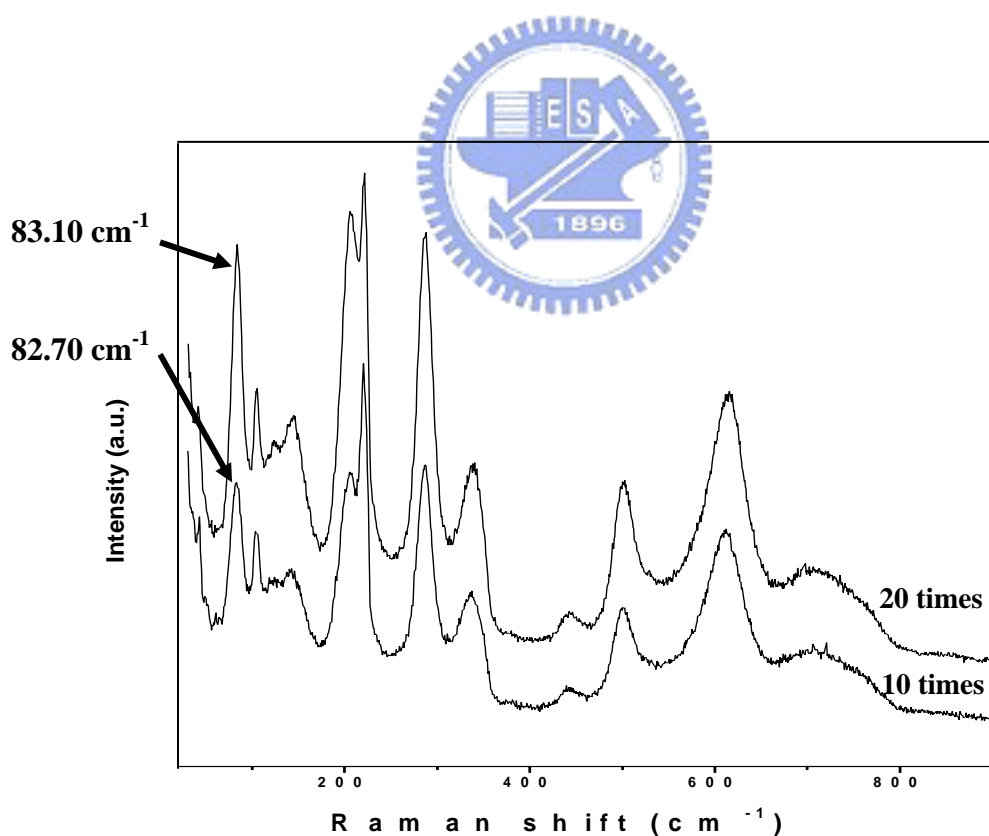


Fig. 4.7 Raman spectra of PTO thin films deposited on Pt/ TiO_2 / SiO_2 /Si substrates with different thicknesses.

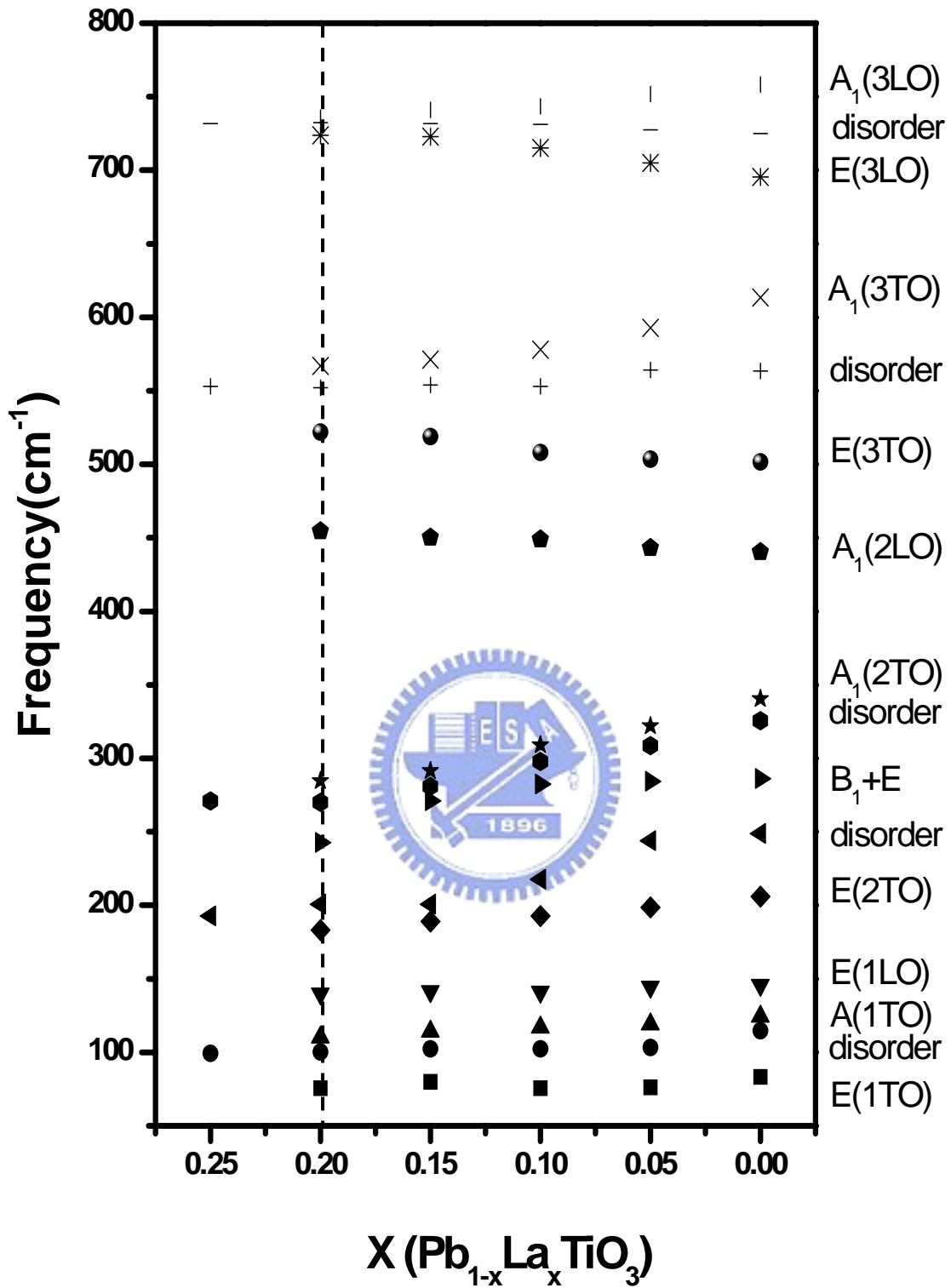


Fig. 4.8 X-dependent phonon modes of $\text{Pb}_{1-x}\text{La}_x\text{TiO}_3$ thin film

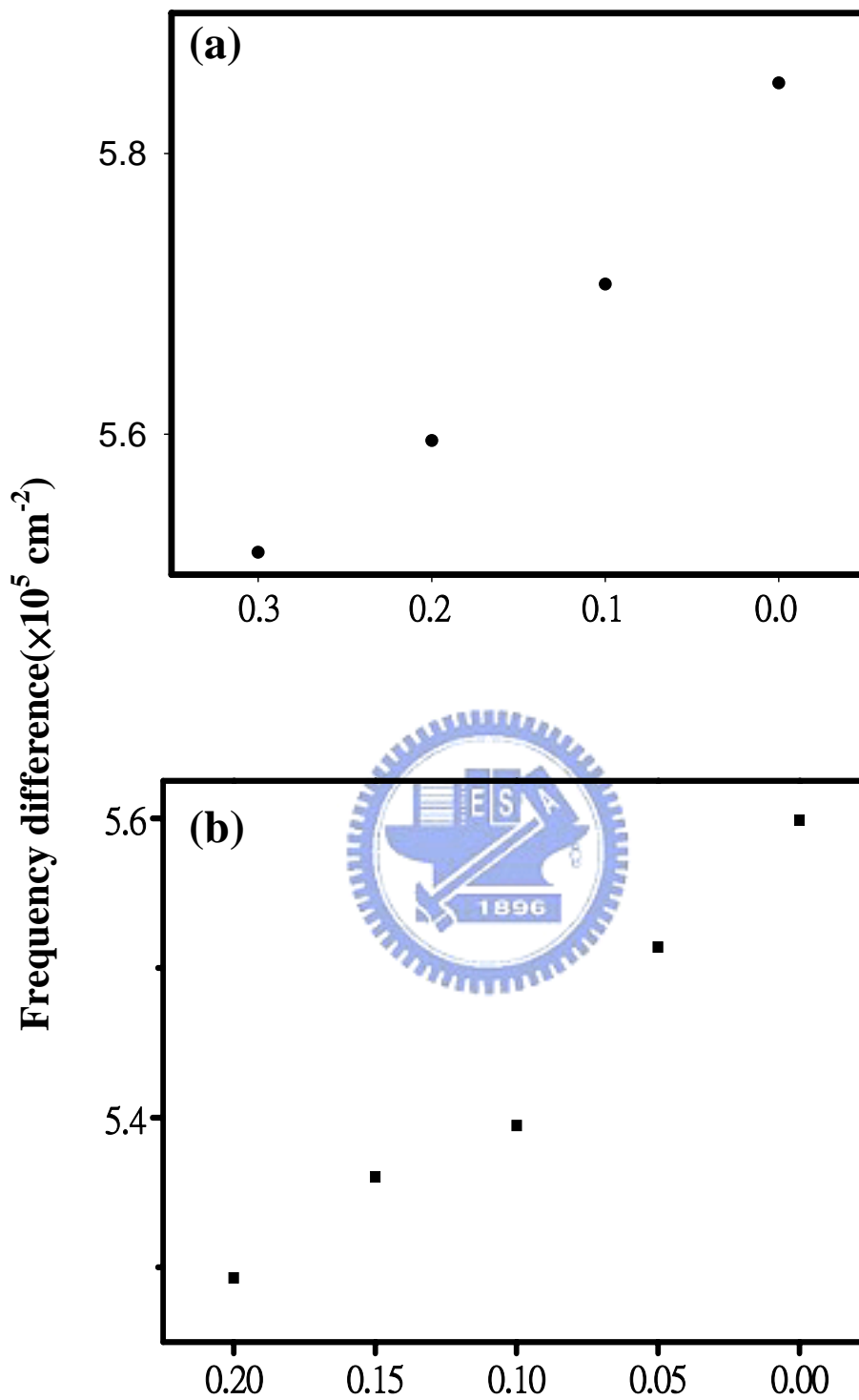


Fig. 4.9 Difference between square of $A_1(3LO)$ and $A_1(1TO)$ phonon frequencies for (a) $\text{Pb}_{1-x}\text{Sr}_x\text{TiO}_3$ and (b) $\text{Pb}_{1-x}\text{La}_x\text{TiO}_3$ systems in tetragonal phase.

4.2 Results of the Er-doped $\text{Pb}_{0.8}\text{La}_{0.2}\text{TiO}_3$ thin films

4.2.1 Results of the X-ray diffraction

The crystalline nature of the films was identified by x-ray diffraction (XRD). Shown in Fig. 4.10(a) are the x-ray diffraction patterns of the $\text{Pb}_{0.8}\text{La}_{0.2}\text{TiO}_3$ thin films doped with Er 3 mol % on the Pt/TiO₂/SiO₂/Si at various sintering temperatures 600~800°C. According to the report of S. Y. Kuo *et al* [14], the BST:Er thin films sintered at 600°C show weak perovskite phase with (100), (110) and (200) orientations and the secondary phase Er₂O₃ and (Ba, Sr)₂Ti₂O₅CO₃ were also found from XRD result.

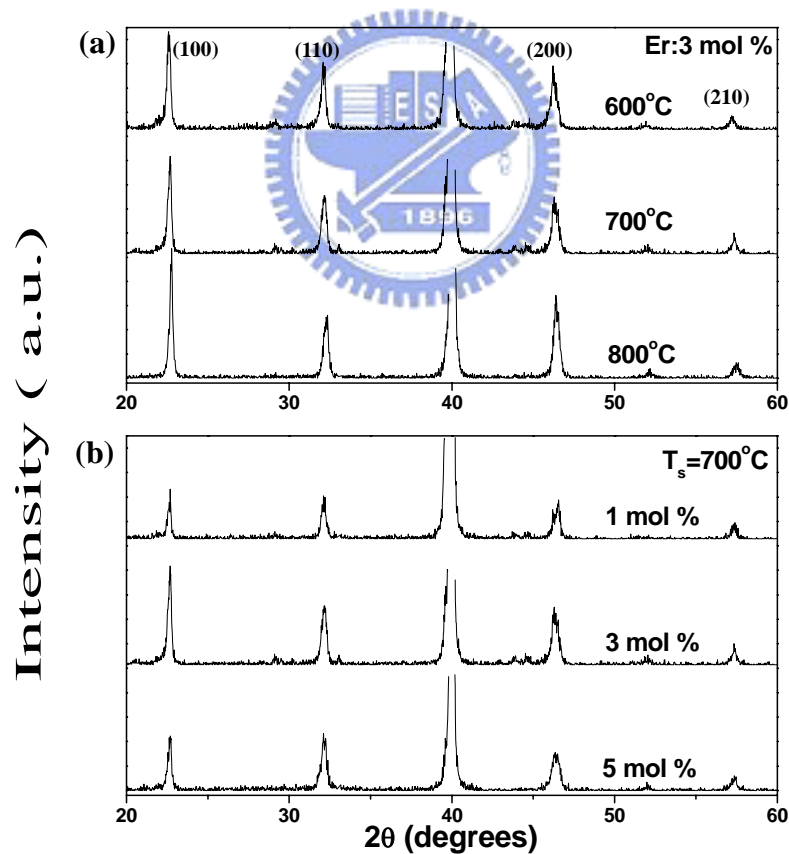
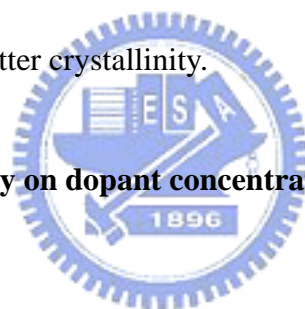


Fig. 4.10 XRD patterns of the Er-doped $\text{Pb}_{0.8}\text{La}_{0.2}\text{TiO}_3$ thin films sintered at various temperatures (a) and doped with various Er concentrations at 700°C.

In the present case, the $\text{Pb}_{0.8}\text{La}_{0.2}\text{TiO}_3$ thin films doped with Er 3 mol % sintered at 600~800°C possess good perovskite crystallinity without the existence of secondary phase. But, the minor line at ~31 degrees that has been ascribed to $\text{Er}_2\text{Ti}_2\text{O}_7$ phase was observed at sintering temperature 600°C.[24,25] The FWHM of the peaks decreased and the intensity strengthened with the increase of the sintering temperature. It indicates that the $\text{Pb}_{0.8}\text{La}_{0.2}\text{TiO}_3$ films doped with Er 3 mol % at sintering temperature 800°C has better crystallinity and the largest grain size (the crystallite diameter:46 nm) and the grain size decrease to 38 nm while the sintering temperature decreases to 600°C. The crystallite size was calculated by using Scherrer's relation. Fig. 4.10 (b) shows the x-ray diffraction patterns of the $\text{Pb}_{0.8}\text{La}_{0.2}\text{TiO}_3$ thin films doped with various Er concentrations sintered at 700°C. It indicates that the $\text{Pb}_{0.8}\text{La}_{0.2}\text{TiO}_3$ films doped with Er 3 mol % has better crystallinity.

4.2.2 Luminescence efficiency on dopant concentration in the erbium-doped thin films



The mechanism of emission of Er^{+3} -contained materials has been well established in the literature [26,27] and the energy diagram is schematically shown in Fig. 2.5. The PL spectra of $\text{Pb}_{0.8}\text{La}_{0.2}\text{TiO}_3$ thin films doped with various Er concentrations are shown in Fig. 4.11 for sintering temperature at 600°C, 700°C, and 800°C under the 488 nm laser excitation at room temperature. The green peaks at 530 nm and 550 nm are attributed to the Er^{+3} inner shell $4f$ $^2\text{H}_{11/2}$ and $^4\text{S}_{3/2}$ to the $^{15}\text{I}_{15/2}$ ground level, respectively. But, the red emission centered at 660 nm ascribed to the $^4\text{F}_{9/2}$ to $^{15}\text{H}_{15/2}$ wasn't observed in this work. Apparently, the shapes of the PL spectra seem the same for the films sintered at various temperatures. It agrees with the result of XRD measurement. The characteristic emission peaks in these films were attributed to the

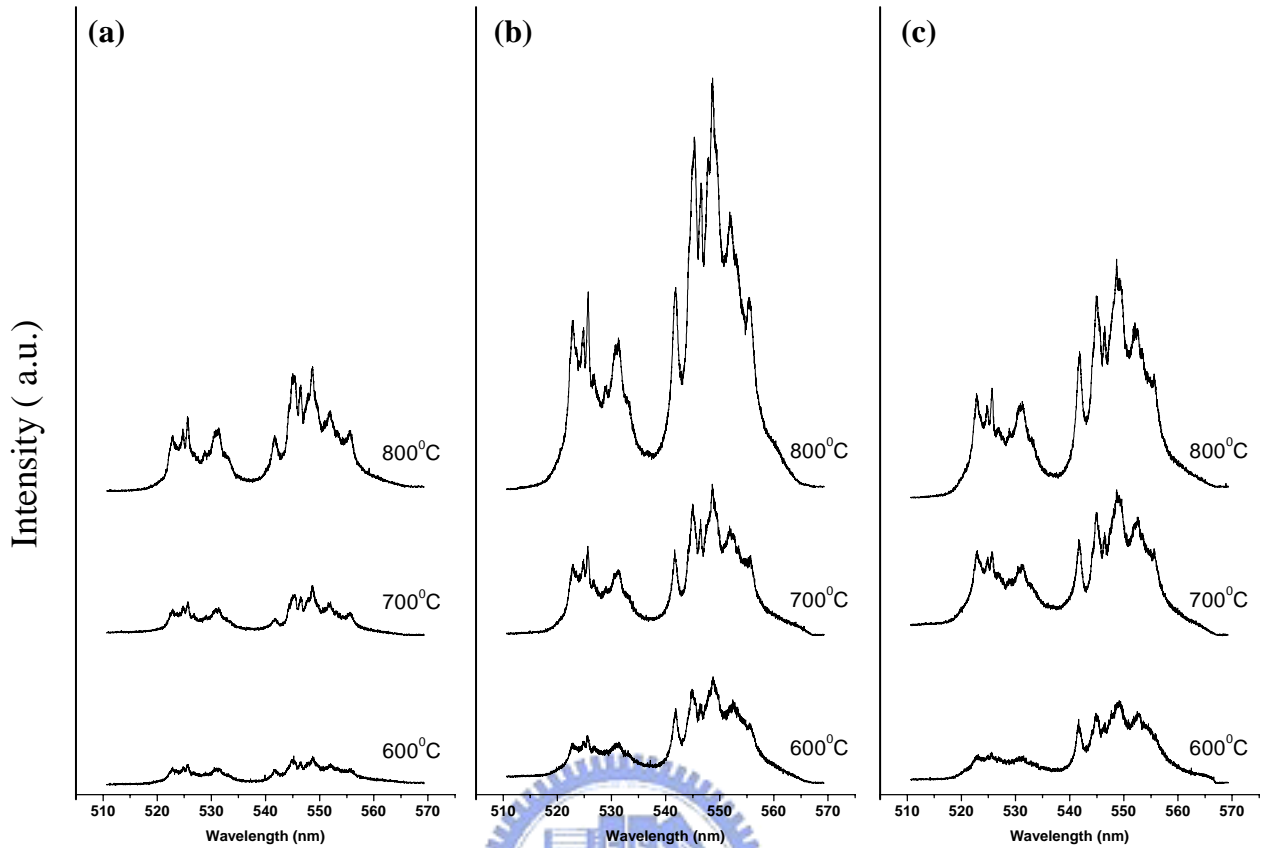


Fig. 4.11 Room temperature photoluminescence spectra from $\text{Pb}_{0.8}\text{La}_{0.2}\text{TiO}_3$ thin films doped with (a) 1mol % (b) 3mol % (c) 5mol % of Er under various sintering temperatures.

Stark splitting of the degenerate $4f$ levels under the crystalline field, and homogeneous and inhomogeneous broadening caused by the film's texture structures and multi-domain structures.

In order to compare the relationship between the green emission and the crystallinity, Fig. 4.12 shows the photoluminescence intensities of the $\text{Pb}_{0.8}\text{La}_{0.2}\text{TiO}_3$ films doped with various molar ratios of Er at different sintering temperatures 600°C , 700°C , and 800°C . The diversity of emission behavior related to Er^{+3} concentration of thin films sintered at various temperatures is apparent. We found that the emission intensities of the PLT:Er films increase as the Er doping concentration increases from

1 to 3 mol %. Meanwhile, the photoluminescence intensities decreases as Er doping concentration exceed 3 mol %. The quenching mechanism is thought to be a cross-relaxation process between two closely placed Er^{+3} ions.[28-29].

For all the Er doping, the green emission intensities at 550 nm increase with the increase of the sintering temperature. Fig. 4.13 shows the dependence of the green emission intensities and the FWHM of the (100) peak on the sintering temperature of the $\text{Pb}_{0.8}\text{La}_{0.2}\text{TiO}_3$ thin films doped with 3 mol % of Er. The green emission intensities increase while the FWHM of the (100) peak decreases. That indicates that the improvement of the crystallinity will enhance the luminescence efficiency.

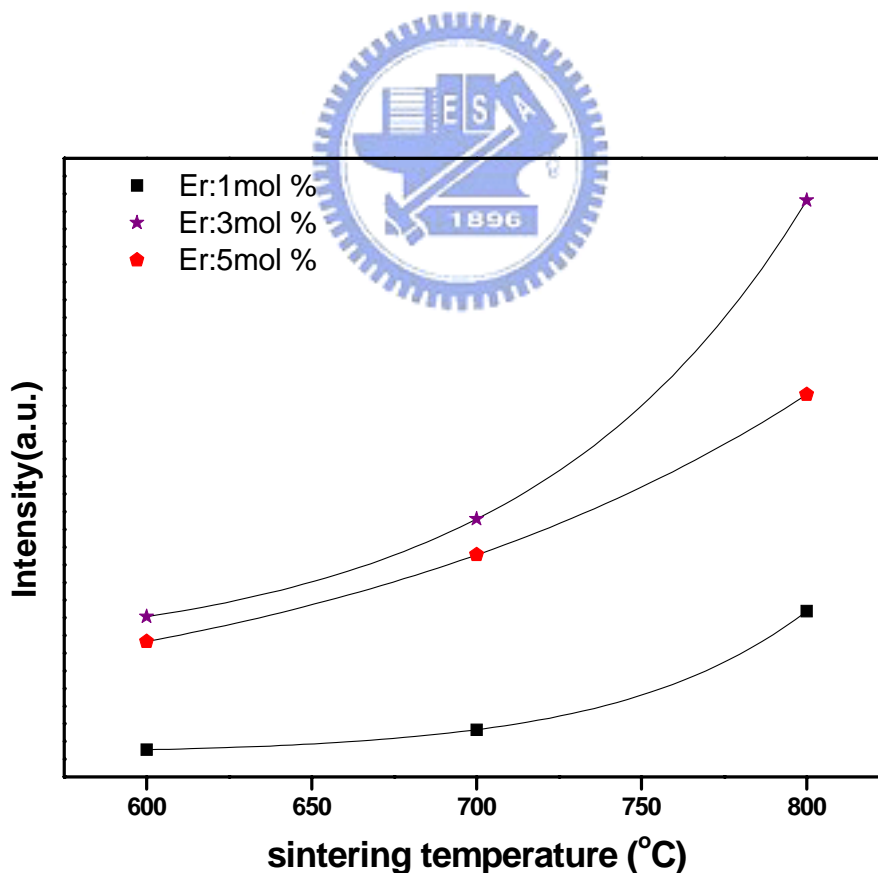


Fig.4.12 Dependence of the green emission intensities of PLT:Er thin films on Er concentration and sintering temperature

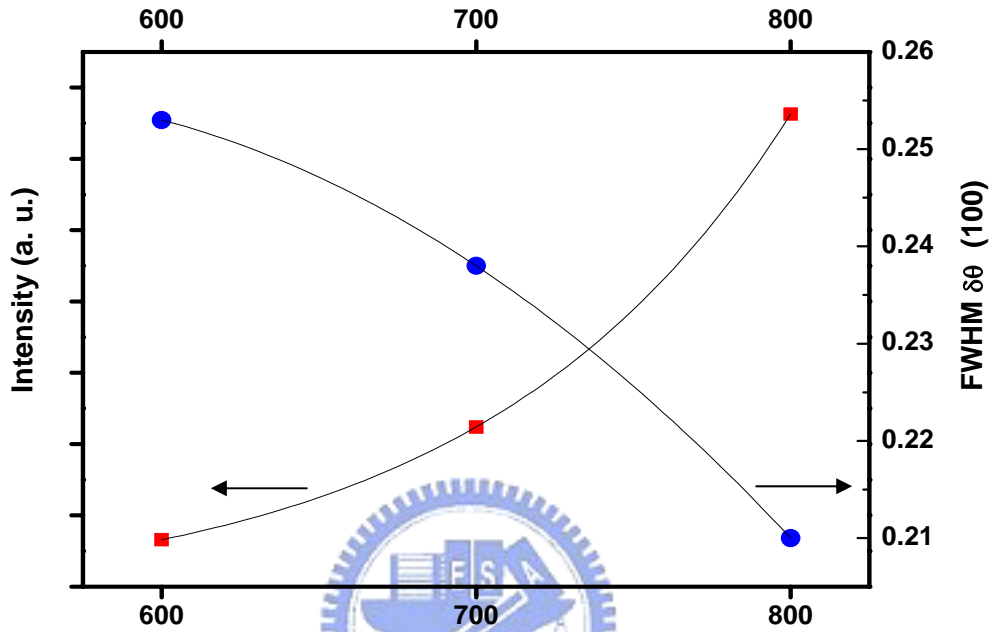


Fig.4.13 Dependence of the green emission intensities (■) and the FWHM of the (100) peak (●) as a function of the sintering temperature of the PLT₃ thin films doped with 3 mol % Er⁺³

Chapter 5

Conclusions

5-1 Conclusion

The main intentions of this work were the study of the lattice dynamics by means of Raman spectra of $\text{Pb}_{1-x}\text{La}_x\text{TiO}_3$ (PLT) thin films and the optical properties by PL spectra of Er-doped films prepared by sol-gel method. All the results and discussions are summarized as follows:

The phase transitions of the samples have been investigated by XRD and Raman spectra. The results of both XRD and Raman measurements of the $\text{Pb}_{1-x}\text{La}_x\text{TiO}_3$ system indicate that there exists a phase transition at $x = 0.20\sim 0.25$, corresponding to the tetragonal-cubic phase. During the course of analyzing the Raman spectra, the Ti-disorder induced background is necessary to be considered. In addition to the identification of phase transition by variation of the lattice constant and phonon modes, we observe the reduced giant LO-TO splitting with the consideration of disorder background. Comparing with the $\text{Pb}_x\text{Sr}_{1-x}\text{TiO}_3$ (PST) system, La^{+3} cations substitution for Sr^{+2} was used in the $\text{Pb}_{1-x}\text{La}_x\text{TiO}_3$ system. The PLT system has the same splitting behavior with PST in spite of the different valence of A-cation substitution and the occurrence of vacancy.

The Er-doped $\text{Pb}_{0.8}\text{La}_{0.2}\text{TiO}_3$ thin films prepared by sol-gel method under various sintering temperatures and dopant concentration have been studied by XRD and PL measurements. Comparing with Er-doped $\text{Ba}_{0.7}\text{Sr}_{0.3}\text{TiO}_3$ thin films, the PLT:Er films show more excellent optical and crystalline properties. We found the PLT:Er films

don't have any obvious secondary phase from XRD at various sintering temperatures. The addition of Er-dopant doesn't down grade the crystallinity of lead lanthanum titanate obviously from the variation of the FWHM of the (100) peak of XRD. The shape of PL spectra is independent of the sintering temperatures and dopant concentration, which is in agreement on the result of XRD. The emission efficiency of PLT:Er thin films was found to be dominated by the Er^{+3} concentration and the crystallinity. The green luminescence intensities of the films reach maximum at 3 mol % Er dopant concentration with the best crystallinity.

5-2 Perspective

Researching on the vibration of the films, it is important to consider the orientation. Because of lacking of the detailed information on phonon mode with orientation, we hope to execute our experiment with the polarized Raman system. Furthermore, we can continue discussing the effect of the Ti-disorder induced background with the same system. In the future work, maybe the phenomenon of vanishing E(1TO) before phase transition will be explained with the description of the electron density distribution by synchrotron radiation.

Although our Er-doped PLT thin films show good performance on both crystalline and optical properties for potential application in photonic devices, we still try to achieve better quality of the thin films by the means of MBE or PLD. Simultaneously, it is necessary for communicated application to measure the luminescence of Er-doped sample at $1.55 \mu\text{m}$ by IR PL.

References

1. S. Bhaskar, S. B. Majmder, P. S. Dobal, R. S. Katiyar, and S.B. Krupanidhi, *J. Appl. Phys.* 89, 5637 (2001).
2. J. Cheng and Z. Meng, *Thin Solid Films* **385**, (2001).
3. C. H. Wang and D. J. Choi, *J. Am. Ceram. Soc.* **84**, 207 (2001).
4. H. Kumazawa and K. Masuda, *Thin Solid Films* **353**, 144 (1999).
5. C. N. R. Rao and K. J. Rao: *Phase Transitions in Soild* (Megrqw-Hill International Book Company, 1978).
6. M. J. F. Digonnet: *Rare Earth Doped Fiber Lasers and Amplifiers* (Marcel Dekker, 1993).
7. J. Heikenfeld, M. Garter, D. S. Lee, R. Birkhahn and A. J. Steckl, *Appl. Phys. Lett.* 75, 1189(1999).
8. H. X. Zhang, C. H. Kam, Y. Zhou, X. Q. Han, S. Buddhudu, Q. Xiang, Y. L. Lam and Y. C. Chan, *Appl. Phys. Lett.* 77,609 (2000)
9. S. M, Takahaashi M, Kanno R, Kawamoto Y and K. K, *Appl. Phys. Lett.* 65. 1874 (1994).
10. J. Heikenfeld, D. S. Lee, M. Garter, R. Birkhahn and A. J. Steckl, *Appl. Phys. Lett.* 76, 1365(2000).
11. W. Zhong, R. D. King-Smith and D. Vanderbilt, *Phys. Rev. Lett.* **72**, 3618 (1994).
12. S. Y. Kuo, W. Y. Liao and W. F. Hsieh, *Phys. Rev. B* **64**, 224103-1 (2001).
13. S. Y. Kuo, Chung-Ting Li and W. F. Hsieh, *Appl. Phys. Lett.* 81, 3019 (2002).

14. S. Y. Kuo, Chin-Sheng Chen, Tseung-Yuen Tseng, S.-C. Chang and W. F. Hsieh, *J. Appl. Phys.* 92, 1868 (2002).
15. S.B. Majumder, M. Jain and R.S. Katiyar *Thin Solid Films* **90**, (2002).
16. R. Resta, M. Posternak and A. Baldereschi, *Phys. Rev. Lett.* 70, 1010(1993).
17. U. V. Waghmare and K. M. Rabe, *Rev. B* 55, 6161(1997).
18. D. Fu, H. Suzuki and K. Ishikawa, *Phys. Rev B* 62, 3125(2000)
19. J. A. Sanjuro, E. Lopez-Cruz, and G. Burns, *Phys. Rev. B* **28**, 7260(1983)
20. G. Burns and B. A. Scott, *Phys. Rev. B* **7**, 3088 (1973)
21. G. Burns and B. A. Scott, *Phys. Rev. Lett.* **25**, 1191 (1973)
22. J. Frantti and V. Lantto, *Phys. Rev. B* **54**, 12139 (1996)
23. C. M. Foster, Z. Li, M. Grimsditch, S. K. Chan and D. J. Lam, *Phys. Rev. B* 48, 10160 (1993)
24. J. H. Hwang, S. K. Choi and Y.H. Han, *Jap. J. Appl. Phys.* 40, 4952 (2001)
25. J. H. Hwang and Y.H. Han, *Jap. J. Appl. Phys.* 40, 676 (2001)
26. C. H. Huang and L. McCaughan, *IEEE Photonics Technol. Lett.* 9, 599 (1997)
27. K. W. Kramer, H. U. Gudel and R. N. Schwartz, *Phys. Rev. B* 56, 13830 (1997)
28. H. X. Zhang, C. H. Kam, Y. Zhou, X. Q. Han, S. Buddhudu, Q. Xiang, Y. L. Lam and Y. C. Chan, *Appl. Phys. Lett.* 77,609 (2000)

29. W. J. Miniscalco, J. Lightwave Technol. 9.234 (1991)

30. I. Taguchi, a, A. Pignolet, L. Wang, M. Proctor, F. L&y, and P. E. Schmid, J. Appl. Phys. 73, 394(1993)

